

The Wolfenstein-Gerstein Effect in Solid Protium-Deuterium Targets


by

Jennifer Maureen Maier
B.Sc., McGill University, 1994.


A Thesis Submitted in Partial Fulfillment of the Requirements for the Degree of
MASTER OF SCIENCE

in the Department of Physics and Astronomy.

We accept this thesis as conforming
to the required standard




Dr. G.A. Beer, Co-Supervisor (Department of Physics)




Dr. A. Olin, Co-Supervisor (Department of Physics)



Dr. J.M. Roney, Departmental Member (Department of Physics)



Dr. C. Bohne, Outside Member (Department of Chemistry)



Dr. P.F. Driessen, External Examiner (Faculty of Engineering)

©J. Maureen Maier, 1997.

University of Victoria


All rights reserved. This thesis may not be reproduced in whole or in part, by photocopy or other means, without the permission of the author.

Co-Supervisors: Dr. Art Olin, Dr. George A. Beer


ABSTRACT

The Wolfenstein-Gerstein effect states that the ratio of the two possible yields from $pd\mu$ fusion ($pd\mu \rightarrow He^+ + \mu^- (5.3MeV)$ and $pd\mu \rightarrow He\mu + \gamma(5.5MeV)$) is dependent on the deuterium concentration of the target. This effect provides a useful way of investigating the multiple processes of the $pd\mu$ fusion cycle by measuring the relative yields of gammas and muons for different target concentrations. By comparing the data to calculations obtained from a kinetics program, it was possible to fit key $pd\mu$ fusion cycle rates, including the gamma branch fusion rates and the muon's rate of transfer from $p \rightarrow d$. Results suggest that the importance of μd emission from the solid target, due to the Ramsauer-Townsend effect, was previously underestimated.

Examiners:




Dr. G.A. Beer, Co-Supervisor (Department of Physics)




Dr. A. Olin, Co-Supervisor (Department of Physics)



Dr. J.M. Roney, Departmental Member (Department of Physics)



Dr. C. Bohne, Outside Member (Department of Chemistry)



Dr. P.F. Driessen, External Examiner (Faculty of Engineering)

Contents

1	Introduction to the μCF Process	1
1.1	μCF in general	2
1.1.1	muonic atoms and muonic molecules	2
1.1.2	the realm of μCF	4
1.2	The fusion cycle	6
1.2.1	formation of muonic hydrogen atoms	6
1.2.2	muonic atoms: The Ramsauer-Townsend effect	9
1.2.3	muonic atoms: hyperfine states and transitions	11
1.2.4	muonic molecular ion formation	12
1.2.5	fusion cycling	14
1.2.6	fusion experiments	15
2	The Wolfenstein-Gershtein effect	17
2.1	Historical development	17
2.2	Previous experiments and theoretical calculations	20
2.3	Present experiment	21
3	The experiment: apparatus and procedure	24
3.1	The beamline	24

3.2	Apparatus	25
3.2.1	the cryostat	27
3.2.2	the target system	29
3.3	Detectors and data gathering	31
3.3.1	the NaI(Tl) gamma detector	32
3.3.2	the conversion μ detectors	33
3.3.3	muon delayed electron detection	35
3.3.4	data processing	36
3.3.5	the trigger	36
3.4	Procedure	40
3.4.1	the gas-rack: measuring gas for a target	40
3.4.2	target depositions	43
4	Presentation and Discussion of Results	45
4.1	Theory: the kinetics code	50
4.2	Discussion	55
4.2.1	μd emission	56
4.3	Errors	57
4.4	Conclusions	59

List of Figures

1.1	μ CF processes in protium, deuterium and tritium mixtures	5
1.2	μ CF in p-d mixtures, including spin states	7
1.3	The Ramsauer-Townsend effect	10
1.4	Theoretical and experimental cross sections for $\mu d_{3/2} \rightarrow \mu d_{1/2}$ on deuterium	13
2.1	The Wolfenstein-Gershtein effect	18
2.2	Theoretical calculation of the ratio of muon yield/gamma yield, with respect to deuterium concentration	23
3.1	The M20B beamline	25
3.2	The target cube from above, showing the positions of the detectors and beam direction	26
3.3	The cryostat	28
3.4	The cryostat inside the target cube	30
3.5	A schematic of the NaI electronics	33
3.6	A schematic of the μ C electronics	34
3.7	A schematic of the del-e electronics	35
3.8	The trigger electronics	37
3.9	A typical ‘good muon’ trigger event	38

3.10	The gas-rack	41
4.1	An example of the gamma energy histograms	47
4.2	An example of the muon energy histograms	48
4.3	The yield ratio plotted w.r.t. c_d	49
4.4	The gamma yield plotted w.r.t. c_d	51
4.5	The muon yield plotted w.r.t. c_d	52
4.6	The $pd\mu$ fusion schematic, including emission	53

List of Tables

1.1	A comparison of spin-flip rates for μd on protium and deuterium	11
1.2	Binding energies of muonic hydrogen molecules	14
1.3	Branching ratios of fusion channels	15
2.1	Previous experimentally measured fusion rates.	21
2.2	Theoretical fusion rates	21
3.1	The calculated target concentrations, including errors	42
4.1	The reaction rates	54
4.2	μd emission probability w.r.t c_d	56

Acknowledgements

It has been an honour and a pleasure to work with so many brilliant physicists and terrific people from all over the world. I've enjoyed this project and will miss the interesting work and great company.

In particular, I owe a lot to Claude Petitjean, Valeri Markushin, Peter Kammel and Slava Bystritski for their never-ending patience, interest and help. Thanks also to the supporting friendship of my fellow grad students, Tracy Porcelli and Makoto Fujiwara, and to Françoise Mulhauser and Roland Jacot-Guillarmod for taking me onto the E742 team.

The University of Victoria has been a great learning environment, with kind and helpful staff and a friendly and encouraging atmosphere. It is fortunate to have remarkable people like my supervisors, George and Art, who made everything look easy, and Glen Marshall, who regularly went above and beyond the call of duty to give me a much needed hand.

Most of all, thanks to my family and Karl, my favorite proof-reader, who willingly learned much more about muons than they ever dreamed possible!

Chapter 1

Introduction to the μCF Process

One of the most universally appealing aspects of nuclear physics is fusion. The quest for the environmentally friendly energy source, renewable and non-polluting, has led to widespread hope that clean ‘fusion-generators’ will someday be possible.

Cold fusion, in particular, has gained a lot of media attention over the past few years. Unfortunately, the relatively successful form of cold fusion, namely muon-catalyzed fusion (μCF), has not attained this level of general popularity. I say unfortunately because it is a unique and exciting field, despite being unable to promise the ‘golden egg’ of unlimited green energy.

By replacing the usual electron of a hydrogen atom with a heavier lepton (i.e. a muon) closely bound molecules can be formed that can spontaneously overcome the inter-nuclear repulsion and fuse. This is the mechanics of μCF . This thesis explores the Wolfenstein-Gershtein effect, which deals specifically with the relative yield of protium-deuterium fusion products.

1.1 μCF in general

Muon catalyzed fusion has long provided a rich field of study in nuclear, molecular and particle physics. It was first predicted by Frank (1947), Sakharov (1948) and Zeldovich (1954) [1, 2, 3]; the first μCF events were reported by Alvarez *et al.* in 1957 [4]. The complexity of the μCF system, although making it a very interesting field of study and providing forty years of exciting research, requires lengthy explanations of its historical background and multiple levels of processes.

1.1.1 muonic atoms and muonic molecules

The muon itself was discovered in 1937. It is a part of the generations mystery; the μ^- is the seemingly superfluous ‘big brother’ to the electron. In total there are three generations of leptons, beginning with the electron (e), followed by the muon (μ) and the tau (τ), where each particle is heavier than that of the preceding generation. The muon is approximately 207 times heavier than the electron; otherwise it generally has the same properties. Like the electron, the muon interacts via the weak and electromagnetic forces, but it is unstable, with the second longest lifetime of any weak decaying particle (i.e. $2.2 \mu s$). When a muon penetrates matter, it is rapidly thermalized and captured, replacing an electron, thus forming a muonic atom. The muon will transfer from hydrogen to the heaviest nucleus present because of the latter’s deeper Coulomb potential. A muonic hydrogen atom may interact with other atoms to form muonic molecular ions. Due to the relative speed of many of these atomic and molecular processes, a single muon may be involved in hundreds of interactions before it decays into an electron and two neutrinos.

Because of the mass difference between the muon and the electron, muonic atoms are approximately 207 times smaller, bound that much more tightly, than ordinary atoms. This can be explained simply using the Bohr model of a hydrogen atom, where the Bohr radius

(in natural units) is:

$$r_{Bohr} = \frac{(m_l + M_p)}{\alpha m_l M_p}$$

with $\alpha \equiv$ the fine structure constant while l represents
either a muon or an electron, and p represents proton

Observe how it depends inversely on the atom's reduced mass ($\frac{m_l M_p}{(m_l + M_p)}$), and thus is decreased by the substitution of a muon for an electron.

Muonic atoms with hydrogen isotopes for nuclei can make diatomic muonic molecules, which is not usually possible for other types of muonic atoms¹. These molecules are, again, on the order of 200 times smaller than regular molecules. This brings the two nuclei in the molecule closer to being within the strong force range, thereby exponentially enhancing the probability of quantum tunneling and spontaneous fusion (except in the case of $pp\mu$ molecules, where the weak interaction dominates, i.e. $p + p \rightarrow d + e^+ + \nu_e$).

The separation of the proton and deuteron in an HD^+ molecule is on the order of 1\AA , which is much larger than the approximately 0.005\AA of a $pd\mu$ molecular ion, but even the latter is much larger than the few fermi, 10^{-5}\AA , where the nuclear forces take over. This does not seem to be a significant enough change to explain why the likelihood of any of the HD^- on earth fusing is less than once in 20 millennia, while $pd\mu$ fusions occur at a rate of 10^6 per second. This difference comes in part from the increased vibrational frequency, a factor of $(\frac{m_\mu}{m_e})^{3/2}$, but mostly from the relative widths of the potential barriers. Even the relatively small difference in size of these two molecules is enough because of the exponential dependence; for a square barrier, tunneling probability depends *exponentially* on the *square*

¹Although it is *possible* to form other muonic molecules, it is *much* more likely for the muon to merely transfer to the heavier isotope instead. Even if a heavier molecule is made, fusion cannot occur in these cases because the greater positive charges of the nuclei will force the inter-atomic distances to be too large for a reasonable probability of tunneling.

of the potential width. For $dt\mu$ molecular ions the increase in rate over a regular DT molecular ion is by a factor of $\approx 10^{77}$ [5]!

1.1.2 the realm of μCF

μCF is useful in the study of low energy (few eV) nuclear processes that cannot be reached in traditional scattering experiments. The range of physics encompassed by μCF includes areas of interest from multiple fields of study:

- astrophysics: the S function (relating to the stellar p-p fusion cycle)
- atomic physics : muonic cascade, elastic and inelastic scattering and transfer processes (including spin exchange)
- molecular physics : resonant and non-resonant molecular formation, bound states
- sub-atomic physics:
 - strong interaction : fusion rates, branching ratios
 - weak interaction : nuclear μ capture

(For an informative survey of these topics, see [6]). μCF is also believed to have potential for other uses— as a source of 14 MeV neutrons, for example[7].

The theoretical side of μCF is also advancing steadily. Recently, due to *ab initio* calculations for 3 body nucleon systems, low energy $pd\mu$ capture reactions were predicted.[8] Although a few elusive problems remain (e.g. the discrepancies in the prediction of spin-flip rates), many of the complicated reactions in the μCF cycle can now be accurately reproduced by theory.

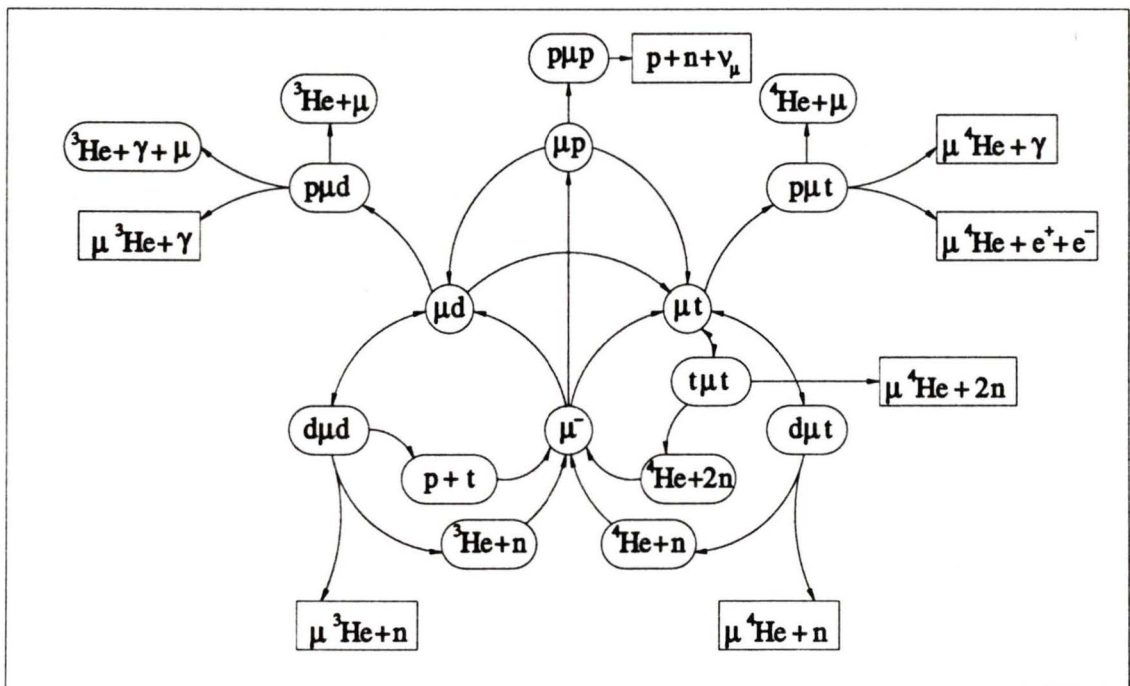


Figure 1.1: μCF processes in protium, deuterium and tritium mixtures; note that final states with square boxes indicate no recycling occurs, while those with rounded brackets indicate that the muon is free to resume the cycle.

1.2 The fusion cycle

The general μCF process illustrated in Figure 1.1 can be described as follows: the μ^- stops in a target and is captured onto a hydrogen atom. If the muon is captured by a protium atom it most likely transfers to deuterium (or tritium) due to the increased reduced mass ($\Delta E(\mu p - \mu d) = 134.7 \text{ eV}$). The formation of a $pd\mu$ ($dd\mu$, $dt\mu$ etc.) molecule may follow and fusion occurs. $pd\mu$ fusion produces a helium nucleus and the fusion energy is carried away by either a photon or by the muon. In the latter case the muon is emitted with 5.3 MeV of kinetic energy (i.e. a ‘conversion muon’²). This muon is free to begin the cycle again. What is more likely is the emission of a 5.5 MeV gamma, while the muon ‘sticks’ to the doubly positive He nucleus, usually ending up tightly bound in the 1s orbital. The muon can decay at any point in this cycle.

Competing processes to $pd\mu$ fusion are muon decay and the formation of other muonic molecules ($dd\mu$ or $pp\mu$). Figure 1.2 shows a model of the fusion process in $\text{H}_2 + \text{D}_2$ mixtures, including the spin states of μd atoms and $pd\mu$ molecules.

To better understand the many reactions and interactions described by the cycle in Figure 1.2, some explanations of the processes are necessary. Below is an outline of muonic cascade, hyperfine transitions (spin-flip), the Ramsauer-Townsend effect, molecular formation and fusion cycling. All of these are important steps to understanding μCF and the Wolfenstein-Gershtein effect.

1.2.1 formation of muonic hydrogen atoms

The Coulomb capture of a μ and its de-excitation is called muonic cascade. It has a very short time scale, of the order of picoseconds, which is substantially shorter than the muon

²The term ‘conversion’ merely refers to the fact that the atom’s energy is ‘converted’ into the kinetic energy of the muon, rather than being lost through the more conventional emission of a photon.

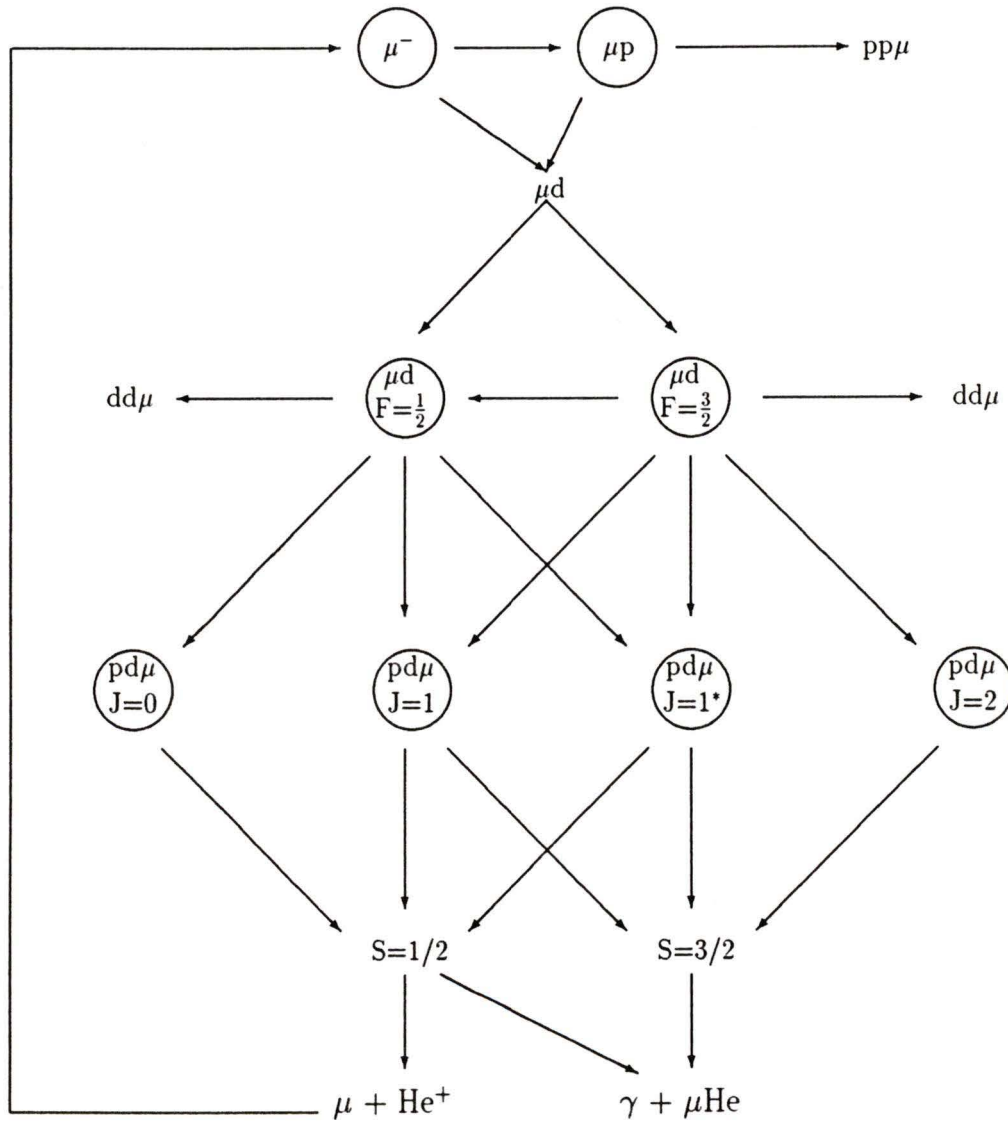
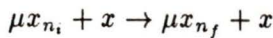


Figure 1.2: The μCF process in protium-deuterium mixtures, including spin states: F =atomic spin, J =molecular spin and S =nuclear spin (i.e. spin of the pd nucleus).

lifetime of 2.2 microseconds. The standard picture of capture is as follows: a muon replaces the electron in an atom by transferring an amount of energy to the electron which is greater than its ionization potential. Comparing the energy of the bound muon in its final state to the energy of the bound electron it replaced, and using $E_n \propto \text{reduced mass} \times 1/n^2$ (where n is the principle quantum number; it defines the energy level of the muon or electron's atomic orbital)³, then $n_\mu/n_e = \sqrt{\frac{m_\mu(M_p+m_e)}{m_e(M_p+m_\mu)}}$. Thus, with $n_e = 1$ for ground state hydrogen, $n_\mu \approx \sqrt{m_\mu/m_e}$ and the muon is initially captured into the $n \approx 14$ atomic orbital.

Because the muonic atom can de-excite to the 1s state through a variety of processes, the energy distributions and populations of the final states are complicated. Possible routes of de-excitation include radiative transition, Auger and Coulomb de-excitation, and transfer to higher Z impurities. Some of the above are dependent on the concentrations of isotopes and/or on the density of the target. Also, some processes are accelerating, providing the muonic atom with extra kinetic energy. This means that not all muonic atoms end up in the usual thermal energy distribution. One example of a process that creates energetic (epithermal) muonic atoms is Coulomb de-excitation, where the muon is transferred from a loosely bound, high energy orbital, to a more tightly bound orbital with a lower energy through a collision with another atom:



with $n_i > n_f$. The energy released is shared between all particles (as all are massive), which gives an acceleration to the muonic atom of up to 75 eV. To further complicate matters, the muon can transfer before it has finished de-exciting. As a result of the complexity of muonic atom formation, effective rates of formation are used, since it is difficult to separate and measure the actual rates individually.

³The complete wave functions and associated energy levels for a charged particle in a Coulomb potential are described in any introductory Quantum Mechanics text.

1.2.2 muonic atoms: The Ramsauer-Townsend effect

Once μd atoms are formed in a protium-deuterium target, they usually thermalize quickly in a target that has a sufficiently high concentration of deuterium; they do not interact as significantly with protium due to the Ramsauer-Townsend effect. Thus the Ramsauer-Townsend effect plays an important role in a concentration- and energy-dependent measurement.

The Ramsauer-Townsend effect was discovered by Faxen *et al.* [9] in low energy scattering experiments on rare gas atoms, and was seen for muonic atoms in a bubble chamber experiment by L.W. Alvarez *et al.* in 1957[4]. The effect itself stems from low energy collisions being dominated by the $\ell = 0$ partial wave, thus allowing the approximation: $\sigma \approx 4\pi \sin^2 \delta_0 / k^2$ (where δ_0 is the phase shift and k the wave vector). Notice that when $\delta_0 = n\pi$, $\sigma \rightarrow 0$. Of course, when the $\ell = 0$ contribution is significantly diminished then the otherwise negligible higher partial waves become the noticeable contributions. In the case of muonic deuterium (μd) scattering on hydrogen, the reduction in the cross section is of the order of 10^2 ; see Figure 1.3.

The scattering amplitude of μd on H_2 is dominated by contributions from the attractive potentials at large distances; these provide the rapid phase change necessary for a noticeable effect (a shift by π is quite significant). The system also has strong repulsive potentials at short distances, but because of their much slower phase changes these repulsive potentials would have to be very large before they could produce the same effect, by which point higher partial waves would contribute[10].

What is important to note from this is that protium is therefore effectively transparent to 6 eV μd atoms, with a macroscopic interaction length for μd on H_2 on the order of a millimetre.

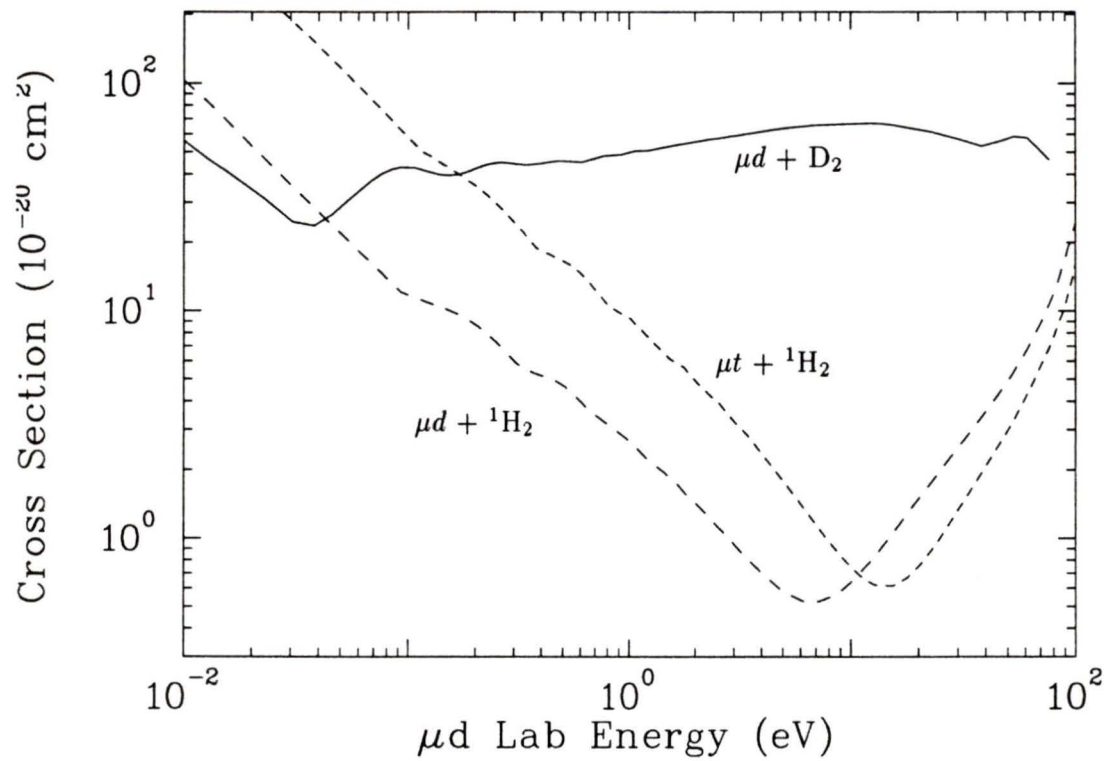


Figure 1.3: *The Ramsauer-Townsend effect: μd cross sections on protium are highly dependent on energy in this region, while that of μd on deuterium is not.*

μd on d $3/2 \rightarrow 1/2$	μd on p $3/2 \rightarrow 1/2$	T=23K
$3.5 \times 10^7 \text{ s}^{-1}$	$5.5 \times 10^2 \text{ s}^{-1}$	

Table 1.1: A comparison of spin-flip rates for μd on protium and deuterium.

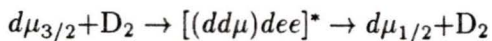
1.2.3 muonic atoms: hyperfine states and transitions

The system of a hydrogen nucleus and a μ^- has two possible spin states; the energy difference between them is called the hyperfine (hf) split. Since the deuteron has a spin of 1 and the spin of the μ is $1/2$, the possible spin states for a μd atom (denoted ‘F’ in Figure 1.2) are $1/2$ and $3/2$. In all three muonic hydrogen atoms (μd , μp and μt) the energy gap, or the hyperfine splitting, of the states is on the order of fractions of eV, with the μd split the smallest at 0.0485 eV.

Under usual experimental conditions, hyperfine quenching (‘spin-flip’ from the $3/2$ to the $1/2$ state) is irreversible. This is an essential element of the Wolfenstein-Gershtein process, as will be shown later. The spin-flip rate itself is quite complicated. It is temperature dependent, and consists of a scattering contribution and an intermediate resonant $dd\mu$ formation portion.

According to theory, hyperfine transitions occur mainly as a result of symmetric collisions (μd on d , μt on t). Non-symmetric collision contributions are relatively insignificant (as shown in Table 1.1).⁴

The other spin-flip process occurs through the formation of a six-body complex (the first step of resonant $dd\mu$ formation, described in the following section) and its subsequent ‘back decay’ to a μd with a different spin state:

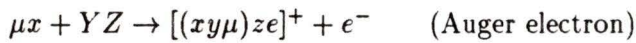


⁴ μp on p requires a relativistic interaction and so has a much smaller cross section.

Evaluating these cross sections involves advanced calculations based on adiabatic expansions of three body Coulomb scattering. These extremely difficult calculations are believed to have an accuracy of better than 10%, but the experimental measurements in Figure 1.4 are almost 40% lower than the theoretical predictions. The formation rates of the various spin states agree and the measured values of $\lambda_{3/2 \rightarrow 1/2}$ do hint at a form that resembles the shape of the theoretical prediction, but the calculated rate of spin exchange is clearly too high. Attempts to locate the source of the discrepancy have resulted in some improvements, but a significant gap remains; the latest theoretical predictions are 20% higher than experimental results [11]. This difference still requires an explanation.

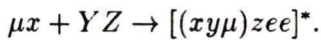
1.2.4 muonic molecular ion formation

Ordinary muonic molecular ion formation proceeds as follows:



where x,y,z (X,Y,Z) are any of p,d or t (H,D or T)

In cases of $dd\mu$ and $dt\mu$ formation there is also a resonant formation process, first proposed by Vesman[19], which results in the formation of a final six-body complex in an excited state:



This process requires the $xy\mu$ molecular ion to have a loosely bound state, so that the final system can absorb the excess binding energy (B.E.) as rotational and vibrational excitation. Because 'ro-vibrational' excitations are on the order of 5 eV, this process has such a strong temperature dependence that it is very sensitive to the kinetic energy of the atoms.

This resonant process is not possible for $pd\mu$ formation, since the $pd\mu$ binding energies

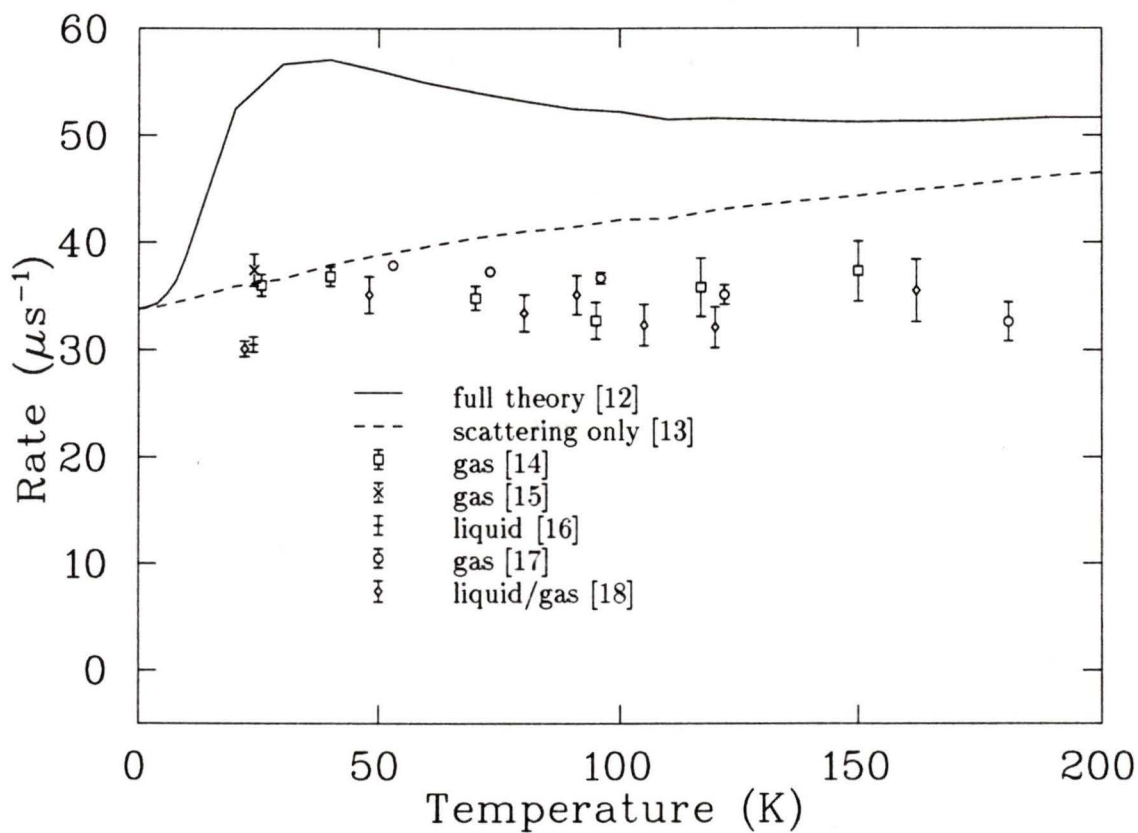


Figure 1.4: *Theoretical and experimental cross sections for $\mu d_{3/2} \rightarrow \mu d_{1/2}$ on deuterium; notice how the complete theoretical calculation of both the resonant and non-resonant contributions (the solid line) is significantly higher than the experimental results.*

State	Binding Energies in eV					
J, ν	$pp\mu$	$pd\mu$	$pt\mu$	$dd\mu$	$dt\mu$	$tt\mu$
0,0	253.15	221.55	213.84	325.07	319.14	362.91
0,1	-	-	-	35.84	34.83	83.77
1,0	107.27	97.50	99.13	226.68	232.47	289.14
1,1	-	-	-	1.97	0.66	45.21
2,0	-	-	-	86.45	102.65	172.65
3,0	-	-	-	-	-	48.70

Table 1.2: *The binding energies of muonic hydrogen molecules. Notice only two states have B.E.s on the order of a few eV. In this table J =orbital angular momentum, and ν is the vibrational quantum number.[5]*

are on the order of 100 eV, as are most of the binding energies of muonic molecules. The only exceptions are for $dd\mu$ and $dt\mu$, where there are two extremely loosely bound states with binding energies of approximately 1-2 eV (see Table 1.2). Resonant formation is still important for the $pd\mu$ fusion cycle and the Wolfenstein-Gershtein effect in particular because of the role it plays in hyperfine transitions, as mentioned earlier.

1.2.5 fusion cycling

Sticking, not the μ lifetime, is considered the main constraint on μCF as a viable energy source. ‘Effective sticking’ is the measure of the number of muons bound to He^{++} nuclei at the end of the fusion chain, minus those stripped off in collisions.

In $pd\mu$ fusion the radiative process (i.e. that produces a gamma and leaves the muon bound to the helium rather than the ‘conversion muon’ branch, where the muon is emitted

J=0	J=1	J=1*	J=2
.84	.872	.986	1

Table 1.3: Branching ratios of gamma (as opposed to conversion muon) fusion events, i.e. $\frac{\Gamma_\gamma}{\Gamma_\gamma + \Gamma_\mu}$: calculated from the data presented in the next chapter. J = molecular spin state

and free to recycle) is favoured with a branching ratio $>84\%$, see Table 1.3. This means that there is little opportunity for cycling in the $pd\mu$ system, while in the $dt\mu$ system the sticking probability is less than 1% [20]. Experiments worldwide have independently reported > 100 fusions per μ in dt mixtures, but this is not possible in the much slower $pd\mu$ fusion process with its low probability of conversion muon fusion.

1.2.6 fusion experiments

Recent experiments in μCF have become more sophisticated, focusing on measuring specific quantities with high precision. Our group has focused on using layered targets of solid hydrogen isotopes to perform the following experiments at TRIUMF:

- E453: measured rate of μd emission as a function of deuterium concentration and thickness
- E613: molecular formation rates of $dd\mu$ and $dt\mu$
- E742: energy dependence of scattering cross sections of μd (and μt) on hydrogen molecules and the Wolfenstein-Gershtein effect

E613 and E742 used a double target system in order to measure the time of flight (TOF) of the μd , or μt , atoms which were emitted from the first target and then travelled across a 20mm evacuated gap to the second target. There they were stopped and their

fusion, transfer, scattering or decay was measured. Since E742 was set up to measure the 5.5 MeV gammas and conversion muons from $pd\mu$ fusion (fusion being a parasitic process to the scattering measurement of μd on protium) it was a natural step to measure the Wolfenstein-Gershtein effect as well.

Chapter 2

The Wolfenstein-Gershtein effect

Although most of the focus is now on $dt\mu$ fusion, because of its relatively high cycling, there is still plenty to learn and measure in the other systems. One interesting phenomenon exhibited in the $pd\mu$ system is the Wolfenstein-Gershtein effect.

In the $pd\mu$ system fusion occurs from four incoherent hyperfine states, with varying combinations of pd nuclear spin ($3/2$ or $1/2$). The distribution of the two possible fusion products, 5.5 MeV gammas and 5.3 MeV conversion muons, is dependent on which nuclear hf state the molecule is in (i.e. $S=1/2$ or $3/2$). S , in turn, is dependent on the molecular hf state (as shown in Figure 2.1). Studying the ratio of the final fusion products can then provide a simple way of separating and identifying some of the many different rates and processes involved in μCF .

2.1 Historical development

Following a suggestion made by Wolfenstein, Gershtein found that, at low temperatures, the hyperfine splitting in the μd atom alters the final distribution of nuclear spins in the $pd\mu$ molecule. As the deuterium concentration increases, so does the spin-flip rate, thus

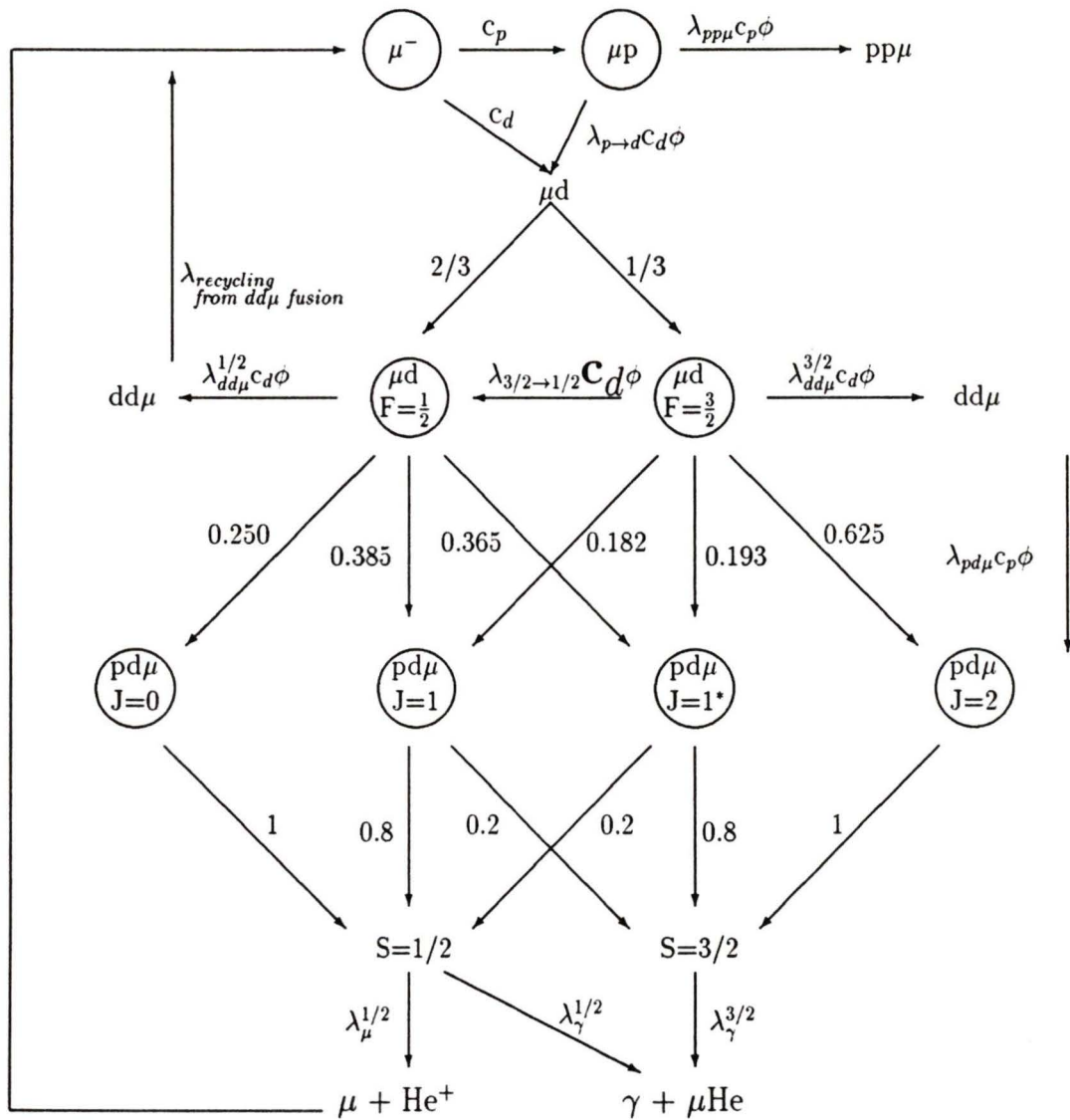


Figure 2.1: The $pd\mu$ fusion process, showing the Wolfenstein-Gershtein effect: spin-flip rates are dependent on deuterium concentration (c_d) and, because all molecular and nuclear spins states are determined statistically, this results in the ratio of fusion products being dependent on c_d also. ($c_p = \text{protium concentration} = 1 - c_d$). ϕ is the density of the target and the λ s are the ‘reduced rates’ of reactions; reduced rates do not depend on concentration or density. Most of the rates are also independent of energy, with $\lambda_{3/2 \rightarrow 1/2}$ being the main exception, as it includes a resonance contribution, as discussed on page 11.

reducing the initial population of the quartet ($S=3/2$) nuclear spin of the $pd\mu$ molecule and enhancing the doublet ($S=1/2$) state. Since the fusion rates depend on the nuclear states, the quartet state only fuses with γ -emission, so having more of the doublet state changes the ratio of gamma to conversion muon yields. The doublet rate is dominant; thus total fusion yield increases with deuterium concentration[21] until the lack of protium atoms significantly reduces the rate of $pd\mu$ molecular formation and $dd\mu$ fusion dominates completely.

Although initial measurements [22, 23, 24] confirmed Gershtein's expected increase in total fusion yield, later calculations and measurements of the spin-flip rate [25, 26] revealed serious discrepancies. This was due to the erroneous 'no-quartet theorem'. Cohen, Judd and Riddell believed that there was relatively small likelihood of fusion from the quartet state (where the nuclear spins are aligned) because of the Pauli exclusion principle and symmetry arguments[27]. They expected that, when the protons in the $pd\mu$ nucleus were in the $S_p=1$ state, it was necessary to flip a spin to produce a transition to the ${}^3\text{He}^+$ ground state (where the protons are in the singlet $S_p=0$ state). These transition rates are smaller than the rates of transitions from the nuclear state with the protons in the singlet state (which don't require flipping a spin) by a factor of $E_\gamma/4Mc^2$, or approximately 1/200. Until 1988 it was therefore assumed that fusion from the nuclear $S=1/2$ state was completely dominant in the pd system. This inevitably led to inconsistent results in the concentration dependence of the yields.

As it turns out, this 'no-quartet theorem' is valid only if one neglects the mixed-symmetry components[8, 28].¹ A few years ago quartet fusion was decisively shown to be

¹Although the total wave function of the two protons must be anti-symmetric because they are identical fermions, the spin of the protons is not limited to being specifically symmetric or anti-symmetric, provided the orbital angular momentum is also of mixed-symmetry. There are combinations of two mixed-symmetry functions that will add to create an anti-symmetric total wave function.[29]

a significant contribution, both in calculation and experiment[8, 30, 31]. Re-analysis of old data confirmed that the experimental data did fit the predictions when fusion from the quartet state was taken into account[31].

2.2 Previous experiments and theoretical calculations

Initial measurements on the Wolfenstein-Gershtein effect were made in gas[23] and, earlier still, in bubble chambers[4, 32, 33]. Relatively recently the radiative yield was measured[30], and old results for the muon yields were recalculated[31], but no single experiment had measured both yields simultaneously.

The theoretical calculations that were compared to our data were performed using accepted values of rates as measured in other recent tests of the Wolfenstein-Gershtein effect. Results from solid target experiments were used where possible (e.g. [34, 35, 36]), but the previously measured values of the fusion rates were from experiments with gas and liquid hydrogen targets.

For the fusion rates, we will refer to the work of Petitjean *et al.*[30] and the recalculations of the previously cited bubble chamber data, as well as data from [24, 37], by Bogdanova and Markushin[31]. The theoretical calculations of these rates were by Friar *et al.*[8].

The experiment done by Petitjean *et al.* used numerous target concentrations of liquid protium and deuterium mixtures, but there were unexpected inconsistencies in evaluating the reduced rates. Although theory suggests these rates are constant, deviations of up to a factor of 2.5 were found; molecular effects and the results of slow thermalization were considered to be the cause. As a result, the final results displayed in Table 2.1 were calculated from the data from targets with $c_d=0.012$ and 0.99 only, where molecular effects were believed to be negligible.

$\lambda_{pd\mu}$	$5.6(2)\times 10^6\text{s}^{-1}$
$\lambda_\gamma^{1/2}$	$0.350(20)\times 10^6\text{s}^{-1}$
$\lambda_\gamma^{3/2}$	$0.110(10)\times 10^6\text{s}^{-1}$

Table 2.1: Fusion rates as measured by Petitjean *et al.*, when $\lambda_\mu^{1/2}$ is fixed at $0.06\times 10^6\text{s}^{-1}$

Bogdanova and Markushin found, using data from [24, 37], that the radiative fusion rate ratio of $\lambda_\gamma^{1/2} : \lambda_\gamma^{3/2} = 3 : 1$, agreed with theory[8]. They also used data from [4, 32, 33] to find: $\lambda_\mu^{1/2} = 0.056(6)\times 10^6\text{s}^{-1}$.

The measurements of Petitjean *et al.* and Bogdanova and Markushin are all in good agreement with theory[8]. These theoretical results are in Table 2.2.

$\lambda_\gamma^{1/2}$	$0.37(1)\times 10^6\text{s}^{-1}$
$\lambda_\gamma^{3/2}$	$0.107(6)\times 10^6\text{s}^{-1}$
$\lambda_\mu^{1/2}$	$0.062(2)\times 10^6\text{s}^{-1}$

Table 2.2: Theoretical fusion rates, according to Friar *et al.*

2.3 Present experiment

Using the previously measured rates, one can predict the relative amounts of each fusion branch for a given target composition. Therefore, indirect measurements of these rates can be made by comparing actual measured yields to the predicted yields.

In our experiment, solid protium-deuterium targets with varying concentrations of deuterium were exposed to the M20B muon beam at TRIUMF. The fusion products, both gammas and conversion muons, were measured, the former in a NaI(Tl) detector and the

latter in a scintillator.

Our measurement is unique, because it measures both products simultaneously, thus allowing us to use a ratio of ratios technique to simplify analysis. The double ratio is useful because it is insensitive to idiosyncracies in normalization and other sources of systematic error.

Valeri Markushin calculated that, at low deuterium concentrations, the population ratio of $F=3/2$ to $F=1/2$ is governed by statistics (2:1). This is because there is effectively no spin-flip and the relative spin populations are constant. At a high deuterium concentration (approximated by $c_d=0.50$) the ratio of $F=3/2$ to $F=1/2$ states is driven down to 0.58:1. This saturation point depends on the competition between the spin-flip rate and the molecular formation rates.

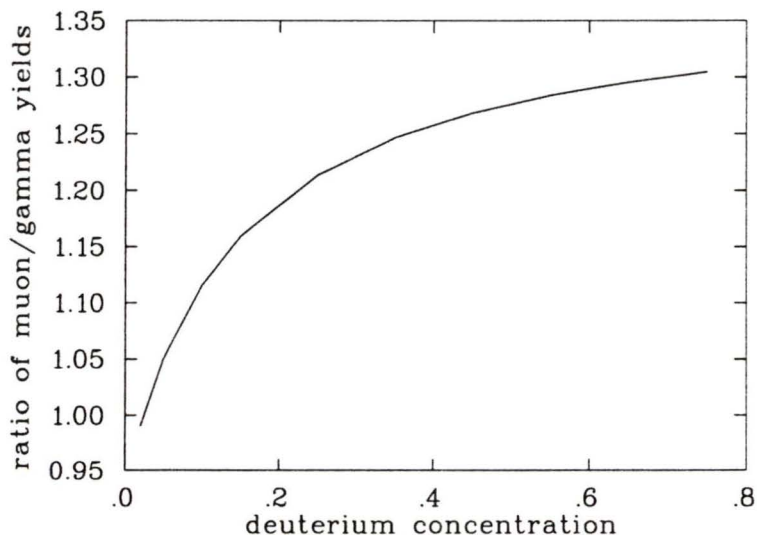


Figure 2.2: *The theoretical curve of the dependence of the ratio of muon yield/gamma yield on deuterium concentration.*

These calculations led to our choice of 2%, 15% and 75% as the three concentrations of deuterium to be used in the targets. It was believed that these three points would

most effectively present comparison with theory at low concentrations, on the steep slope before saturation, and well after saturation was expected to occur (see Figure 2.2). Due to the Ramsauer-Townsend mechanism, targets with concentrations lower than 2% were expected to create a large percentage of non-thermalized μd atoms, many of which would escape from the target before fusion could occur; therefore homogeneous targets of higher concentrations were chosen to simplify the analysis by allowing for assumptions of thermal energy distributions and negligible emission rates.

Chapter 3

The experiment: apparatus and procedure

In this chapter we explain how the data were acquired, and detail the equipment used. A brief outline of the target apparatus is followed by descriptions of the detectors used specifically in measuring the Wolfenstein-Gershtein effect, along with logic diagrams showing how the data were collected and processed. There is also an explanation of the mechanics of target mixing and deposition. The general procedure, and some interesting observations about specific runs, conclude this section.

3.1 The beamline

This experiment was carried out in the M20B leg of the meson hall at TRIUMF, which is depicted in Figure 3.1.

The primary beam of $140 \mu\text{A}$ unpolarized protons at 500 MeV, struck an approximately 10cm Be target to produce, from the surface of the target, the secondary beam of pions that decay into muons. The beam μ^- were selected to have a momentum of $27.0(\pm 0.2) \text{ MeV}/c$,

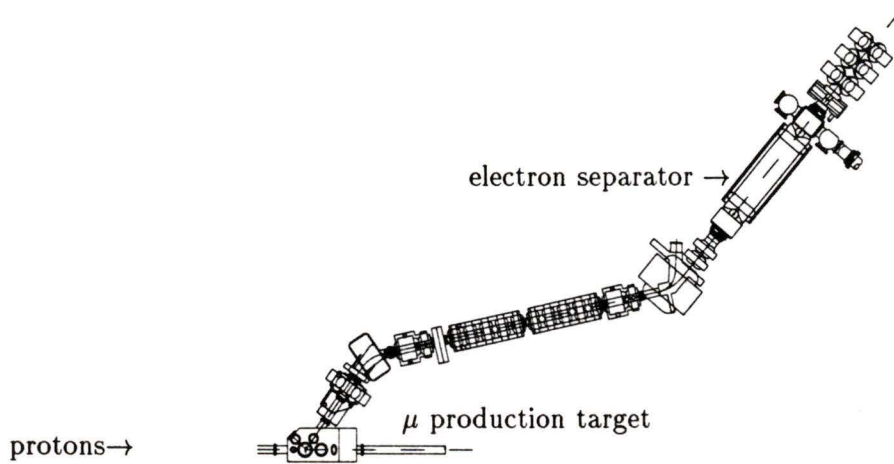


Figure 3.1: *The M20B muon channel: the two beam benders and the separator focus the beam and remove electrons. Using the separator has been known to change the e^- to μ^- ratio from 140:1 to 1:2 [34].*

with a rate of 5×10^3 in a 4cm diameter, and $\delta p/p \approx 4\%$ (or .04 FWHM).

The bending magnets and separator were essential in screening out electrons and pions from the beam. Crossed electric and magnetic fields were used as momentum and velocity filters, thus removing the majority of the electrons that otherwise would have greatly outnumbered the muons.

3.2 Apparatus

As shown in Figure 3.2, the μ beam triggered a 0.127mm scintillator (T1) before entering the target vacuum space through a 0.025mm stainless steel vacuum isolation window. Most muons stopped in the solid hydrogen target, its 0.051mm gold support foil, or the cryostat heatshield. For those muons that captured and fused, the emitted 5.5 MeV gammas were detected with a NaI(Tl) detector, while the 5.3 MeV conversion muons were observed with

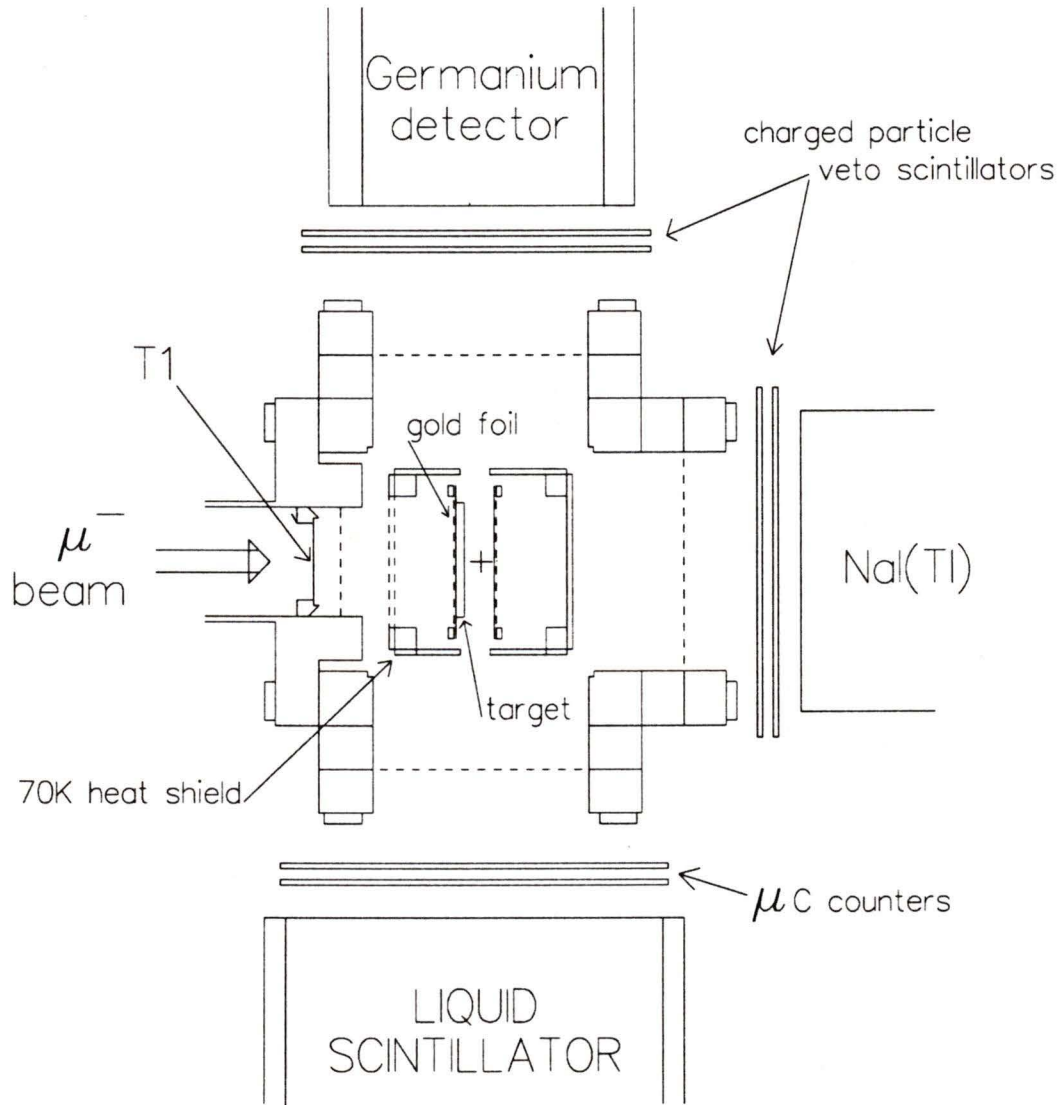


Figure 3.2: The target cube from above, showing the positions of the detectors and beam direction. Notice T1, the trigger scintillator that was used to discriminate against electrons. the muon scintillators on beam right facing the $30\mu\text{m}$ port and the sodium iodide crystal for detecting gammas, behind the 3mm downstream port. The target area inside the cube is shown with the gold target foils and an upstream target in place.

one of the scintillator arrays. The helium ions produced by $p\mu$ fusion were too low in energy (a few hundred keV) to register in any of the available detectors. The liquid scintillator neutron detector was used to observe the signature neutrons of $dd\mu$ fusion events; the germanium detector was used to measure x-rays from muons transferring to high-Z contaminants. The individual details of the target and detectors will be explained later.

The stainless steel cube that surrounded the target area had three ports, one on each vertical face (with the beam entrance as the fourth). The space above contained the cryostat. The diffuser, which deposits the gaseous targets, was housed below (see Figures 3.2 and 3.4). Each port facing a detector was fitted with a thin stainless steel window. These varied in thickness from $30\mu\text{m}$ for the beam right and $50\mu\text{m}$ for the beam left side windows to 3mm for the one downstream. This evacuated area was pumped with a turbo pump backed by a spiral and bellows roughing duo (the entire vacuum space, with pumping lines, the target area and mixing volumes are explained later, when providing an explanation of target preparation and deposition).

3.2.1 the cryostat

One of the unique features of this measurement was that it was made with solid targets; it therefore also required a unique target area design. The key element of this is the cryostat, of which the greater part was built in 1991/92 by a doctoral student, Paul Knowles.

The cryostat consisted of the supporting structure for the target vacuum space and the foils on which the targets were deposited, as well as the cryogenic system that provided the cooling necessary to maintain a target at 3K and the surrounding heatshield at 70K. Figure 3.3 displays the layout of the cryostat.

The liquid He was extracted from a dewar using a transfer line equipped with a needle valve to regulate the flow. The liquid helium was then brought through the top of the

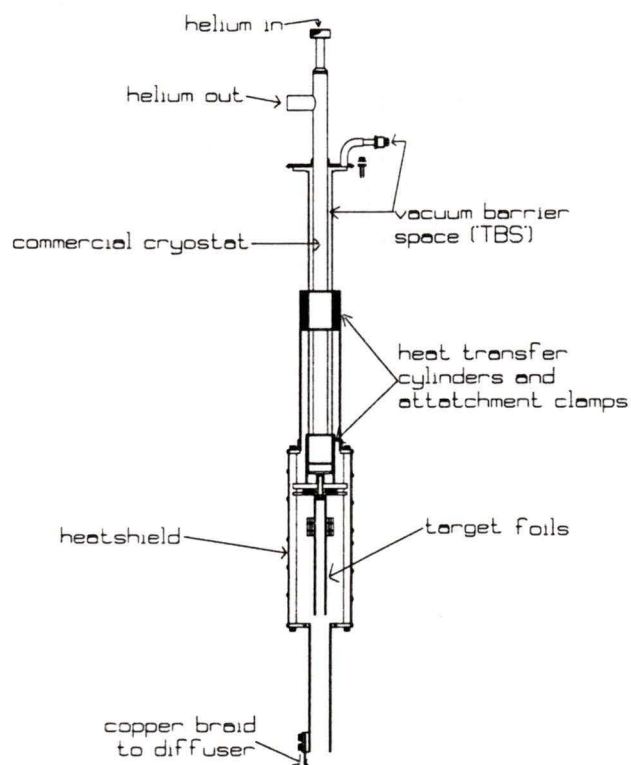


Figure 3.3: *The cryostat: a 70K heatshield surrounding a 3K core suspending two gold foils. The top of the diagram shows where the liquid He was drawn in and the gas pumped out. This upper end of the apparatus was enclosed in a stainless steel cylinder that provided a vacuum barrier space to isolate the area containing helium from the target vacuum area. The outlet from which this space was pumped is clearly visible, top right. A gold plated heat shield surrounded the lower, target portion of the cryostat. A copper braid provided a thermal connection from the bottom of the cryostat to the diffuser through which the target depositions were made. Its flexibility was important, because it was necessary to retract the diffuser from between the foils while data was collected.*

cryostat into a low pressure volume where it expanded and cooled. A pump continually removed the helium gas, keeping the pressure low to maintain the cooling process. This apparatus was purchased from a local company specializing in cryogenics¹.

Thermal connections to the target area were made by clamping copper cylinders and indium between the cryogenic unit and the support that suspends the gold foils. The surrounding heatshield was connected to the cryogenic unit in an identical fashion, except that the conduction paths were designed to keep the heatshield at 70K and the target supports at 3K.

There were various resistor and diode temperature monitors on the cryostat as well as the target foil support arms which monitored the target status and ensured a stable deposition environment.

With the cryostat cooled, a target area vacuum of 10^{-9} Torr could be reached.

3.2.2 the target system

This specialized target design for μCF studies was stumbled upon by accident during a test of emission of μp atoms from solid hydrogen. When an unexpectedly large number of emitted hot (energetic) μd atoms were observed, the idea of a neutral muonic atom beam for use in μCF was born.

The double target system consisted of a cryostat with two arms, each supporting a circular gold foil at beam level (see Figure 3.4). The distance between these target arms was variable, within limits, but it was preset for each experiment. For this run the foils were 20cm apart. The diffuser through which the gas was released in making the solid targets ran on vertical tracks which permitted its insertion between the foils during deposition and its removal during runs (see Figure 3.4). It had two isolated sides, with separate lines that led

¹Quantum Technology Corporation, Whistler B.C.

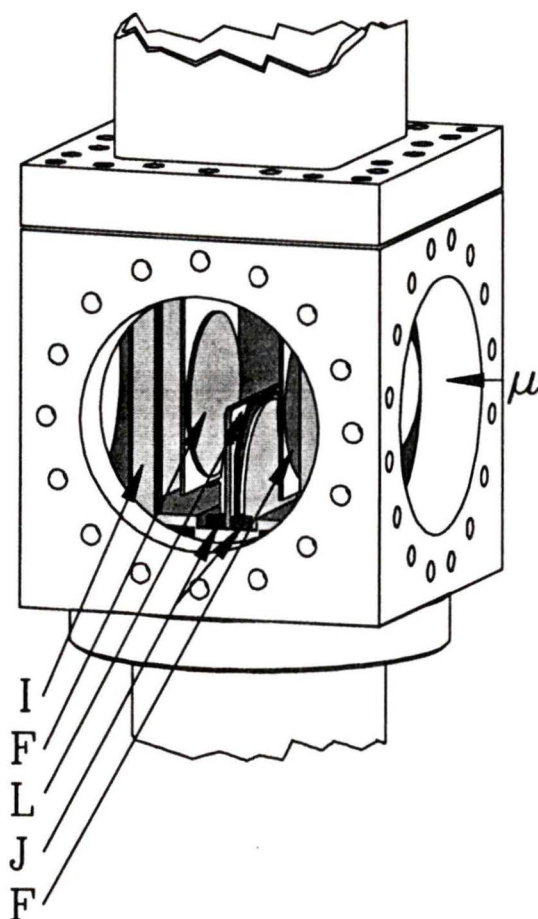


Figure 3.4: *The cryostat inside the target cube, showing the beam direction as well as the interior detail: I= Inside of the heatshield, F= gold foils, L points out the partially inserted diffuser, and J is the end of the track by which the diffuser may be inserted for target depositions.*

independently to the gas mixing volumes. The gas was sent to only one side of the diffuser at a time, and exited the diffuser through a disk of sintered material with $2\mu\text{m}$ pores, at which point it condensed predominantly on the adjacent cold (3K) foil with an efficiency of $87(\pm 8)\%$ [20].

Using this system, it was possible to create targets on both foils, with layers of different gas mixtures (e.g. pure D_2 on top of an HD mixture, or neon underneath H_2). These overlayers have been used for a variety of purposes, including degrading the energy of emitted μd (or μt) atoms.

This system of two targets was useful for time of flight (TOF) measurements, where the energy of the fusing muonic hydrogen atom was found by recording the time interval between the muon's arrival through T1 and the detection of the fusion products. However, this TOF technique was not necessary for the measurement of the Wolfenstein-Gershtein effect.

All of the runs analysed in this thesis had a single, homogeneous target on the upstream foil only. The targets used were all 2000 Torr-litres(Tl) which in this system was equivalent to $7\text{mg}/\text{cm}^2$ for pure protium and $14\text{mg}/\text{cm}^2$ for deuterium, or about 0.8mm thickness — enough to ensure that most of the 27 MeV/c muons were stopped in the target. The concentrations of deuterium (c_d) used in the three targets made specifically for this measurement were $c_d=0.75$, 0.02 and 0.15. A description of how these targets were measured and mixed follows.

3.3 Detectors and data gathering

As seen previously in Figure 3.2, there were four different kinds of detectors used in this experiment: a germanium detector to observe muonic x-rays after capture to heavy nuclei, a liquid organic scintillation detector for measuring neutrons from $dd\mu$ fusions, double scin-

tillator arrays to detect charged particles and conversion muons, and a sodium iodide (NaI) crystal for measuring gamma rays from radiative fusion. The latter two were used to collect the data to be presented in the following chapter.

3.3.1 the NaI(Tl) gamma detector

The crystal used measured approximately 6" in diameter by 6" long.

The NaI(Tl) detector was situated downstream from the target, in the line of the beam. Therefore it received a larger number of background electrons than the other detectors. It was not expected that many muons would pass through the entire target, the 3mm window and the scintillators to reach the NaI detector, although the charged particle veto counters should ensure that this does not affect the gamma spectra. Possible backgrounds were *bremstrahlung* from muon decay electrons, and neutrons from $dd\mu$ fusion.

the NaI(Tl) electronics

The electronics for the sodium iodide, the germanium and the liquid scintillation neutron detectors were, in principle, quite similar. The circuit provided a charged particle veto (provided by the scintillator pair in front of the NaI detector) and basic energy discrimination for the signal before having its timing read by a TDC and its energy read into an ADC (see Figure 3.5). The NaI signal was also used as TRG3 in the trigger electronics, which enabled the general detector coincidence (EVTR) and indicated to the computer that there were events to read out of the ADCs and TDCs.

3.3.2 the conversion μ detectors

The conversion muon detection was accomplished in an array of two standard 8" by 8" scintillators separated by approximately 1mm and each with a thickness of nearly 1/8".

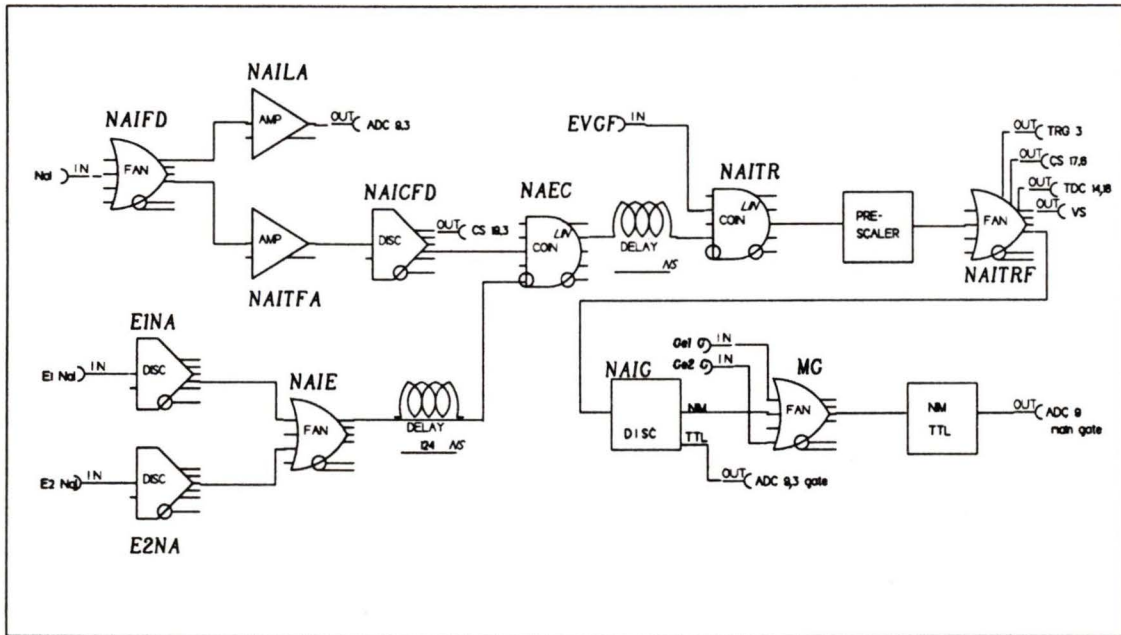


Figure 3.5: A schematic of the NaI electronics: after passing an energy threshold (NAICFD), and an anti-coincidence with the signals from the scintillators placed before the NaI detector to veto charged particles (NAEC), the NaI signal was sent to a coincidence with the event gate (EVGF). The processed signal was then prescaled, and sent from NAITRF to the trigger electronics as TRG3 and the master gate (MG) for the detector ADC. The energy signal was read directly into an ADC, without discrimination, while the timing signal was sent to a TDC from NAITRF.

A muon entering the conversion muon (μC) scintillators would be expected to stop in the first of the pair (E1), leaving a large amount of energy there. Thus, should a particle register in BOTH scintillators (E1 and E2), it was an electron and this signal was vetoed from being counted in the μC histograms. The muon's energy, entirely deposited in E1, was read out by an ADC, and its time recorded by a TDC, as shown in Figure 3.6.

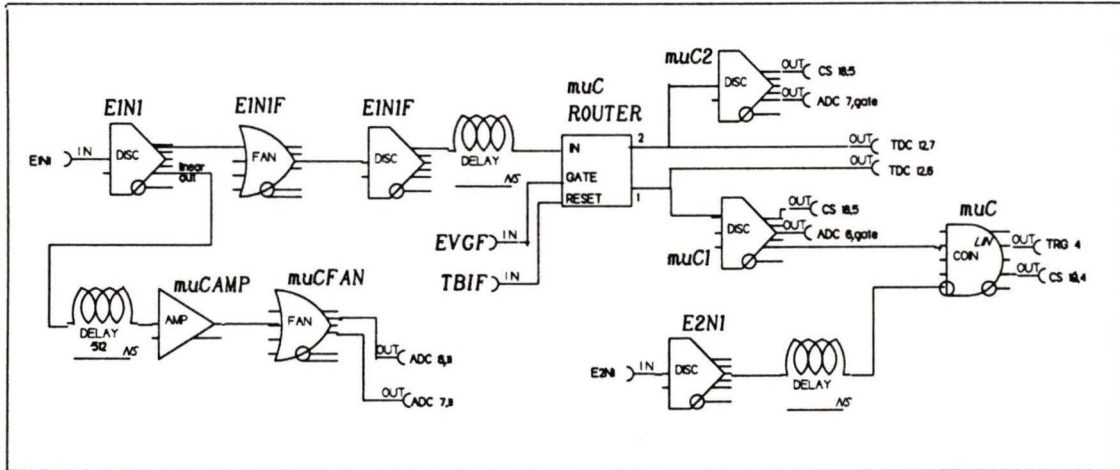


Figure 3.6: A schematic of the μ C electronics, showing the router that sorts the outputs from E1. The router ensures that the initial muon signal was kept separate from the signal left by its decay electron, with the muon signal going on to a TDC and the E1 ADC gate, as well as to make an anti-coincidence with E2 which flags TRG4.

the conversion μ electronics

The output from the first scintillator, E1, was sent through a discriminator and then to a router where the gate is provided by EVGF. The router's purpose was to sort signals; if two signals arrived in the same event window, the first went to output one (this would be the muon stopping), and the second to output two (this would be from the decay electron and can be used as a condition to clean up the muon spectra). The first router output, i.e. the conversion muon signal in which we were interested, was sent to TDCs, to gate the ADCs, and made an anti-coincidence with the delayed, discriminated signal from the second scintillator, E2. This vetoed signal became the start for a detector TRG4 gate in the trigger electronics (again providing an EVTR coincidence, which permitted the recording of the conversion muon event).

3.3.3 muon delayed electron detection

Requiring an event to include the detection of a muon decay electron is an effective background suppression technique. Neutrons and gammas can be produced in nuclear muon capture onto gold or other cryostat materials as well as in $pd\mu$ fusion, but in the former cases the muon is consumed and does not decay into an electron.

delayed electron electronics

Coincidences in any pair of veto scintillators that arrived between 0.2 and 5.05 μs after a candidate fusion event had been observed were identified as delayed electrons (see Figure 3.7). After prescaling, it also was a detector trigger, TRG5, which provided for a coincidence in EVTR.

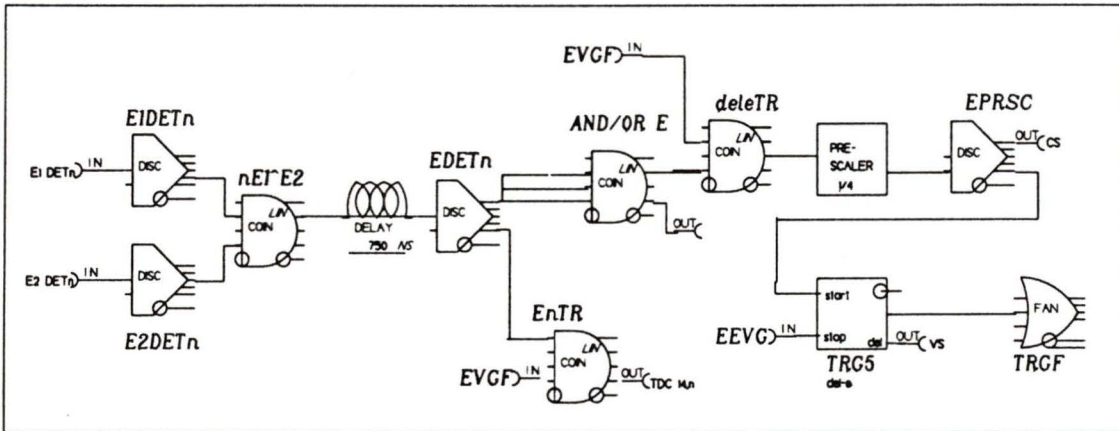


Figure 3.7: A schematic of the del-e electronics, showing how signals from each pair of scintillators were sent to a coincidence and then through a discriminator, $EDET_n$. The ‘n’ represents the label for each of the three scintillator pairs (Ge, N and NaI, indicating which detector the pair preceded). They were then summed (AND/OR) and their coincidence with the event gate (EVGF), prescaled by a factor of four, was used as the start in the TRG5 gate for the trigger electronics.

3.3.4 data processing

The previous sections detail the processing electronics of the NaI(Tl) gamma detector and the conversion muon scintillators. After being pre-processed by these electronics, the signals were then fed into a micro-VAX station via CAMAC, which used a STARBURST front-end processor. The buffered event streams were written to 8mm tape and analysed by the MOLLI histogramming program.

MOLLI, having obtained the detector information from the CAMAC ADCs and TDCs, sorted the events, combining data from different inputs as instructed by the histogram definition program, (e.g. a fusion gamma signal with a delayed electron requirement), and stored the selected information in histograms.

The trigger electronics describe how STARBURST and VDACS communicated with the data gathering electronics.

3.3.5 the trigger

The trigger, which signaled a muon entering the target region, was essential in overcoming the background of electrons and in providing accurate timing of events. The T1 scintillator at the beam entrance window measured the deposited energy of the incoming particle; its threshold was set to detect slow muons and discriminate against fast electrons. If the incoming particle succeeded in triggering T1, and if there was no inhibit from a 'computer busy' or due to an event trigger, a time zero was set and the system was enabled to receive events from any of the detectors.

Figure 3.8 gives a complete layout of all the trigger electronics, while Figure 3.9 simplifies the explanation of the timing. The signal from T1 was discriminated to eliminate the electron events by demanding the energy deposited in T1 by an incident particle be greater than the minimum energy deposited by a muon with the desired momentum of 27

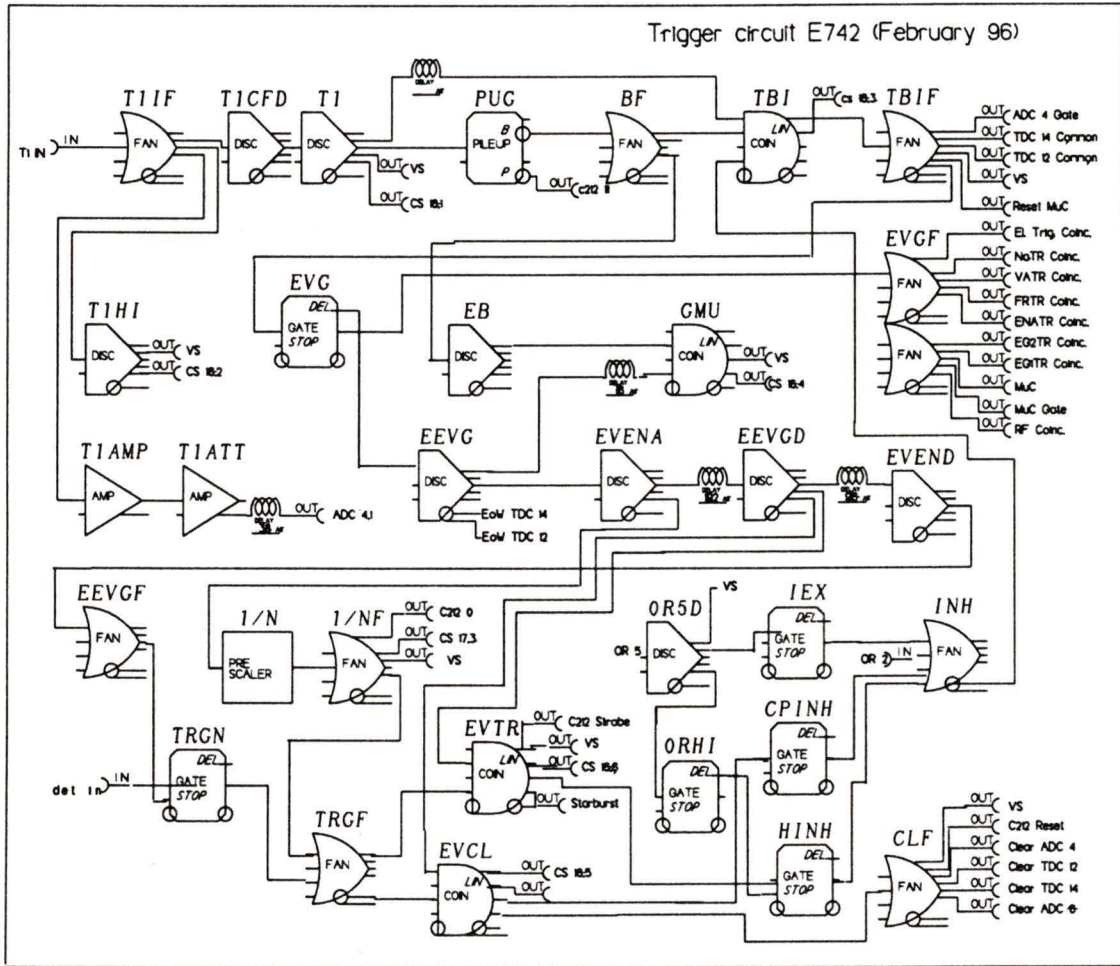


Figure 3.8: The trigger electronics: which displays how the arrival of a muon in T1 opened a timed event gate, during which the system was open to accept events from each of the detectors. If a detector did register an event in this window, it fired TRGn, which flagged the event trigger, EVTR, to call on the computer to read out the data collected in the ADCs and TDCs.

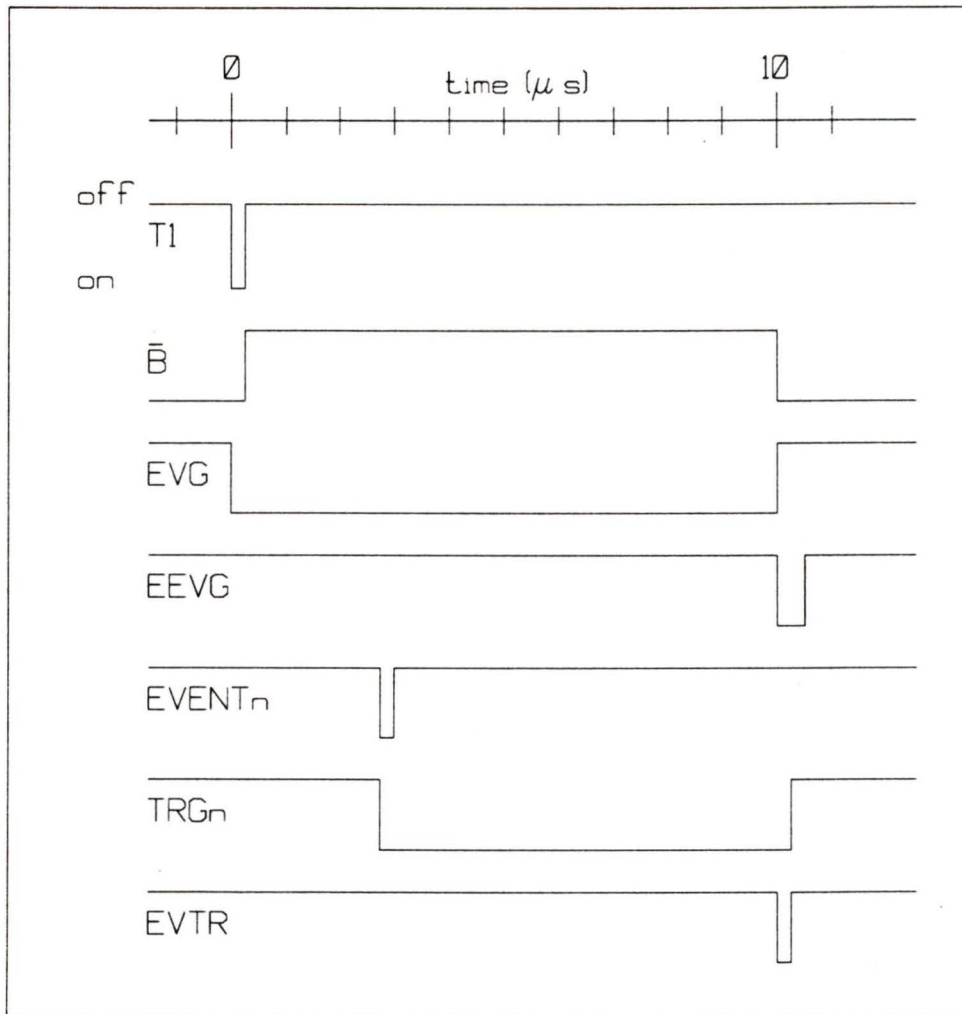


Figure 3.9: This example explains the logic and timing of an accepted ‘good muon’ trigger event with a detector event arriving from that muon. Because there was no inhibit (not shown: \overline{INH} is on until $EVTR$ turns it off) when $T1$ fires, and the not-busy \bar{B} is timed to turn off just after $T1$ arrives at the $T1$, \bar{B} , \overline{INH} coincidence, then the event gate EVG is created. No second muon arrived during the event gate to cause a ‘pile-up’ and extend \bar{B} , so \bar{B} is back on when $EEVG$ arrives at the ‘good muon’ (GMU) coincidence. When $EEVG$, the end of the event gate EVG , coincides with the detector trigger, TRG_n , it produces a coincidence in $EVTR$, the event trigger. Note: the short pulses have been extended in length to make the coincidences easier to see.

MeV/c. This turned off the pile-up-gate output (\overline{B} for not busy) for $10 \mu\text{s}$, indicating that the system had accepted a muon. If a second arrived during this gate it was a ‘pile-up’ event and extended the busy output to $10 \mu\text{s}$ after the last muon arrival; the software was designed to dismiss all data from these events.

The ‘acceptable event’ gate was opened when a signal came from T1, and there was no pile-up and no-inhibit from the computer (indicating that STARBURST and VDACS were ready to accept data).² This coincidence also provided a common start for the CAMAC TDCs.

The event gate indicated the period of time after the arrival of a muon when a detector event would be expected to come from that muon. A coincidence between the end of the event gate (EEVG) and any trigger event (TRGF) defined a general event trigger (EVTR), while no coincidence resulted in an event clear (EVCL). If there was an event trigger, the hardware inhibit (HINH) and then the computer inhibit (CPINH) were activated so the ADCs and TDCs ignored any new data until the data they already held were read out by the STARBURST and then cleared. An event clear (no detector and event coincidence) would skip the readout step and simply set the inhibit (CPINH) while clearing the modules.

As well as recording the time and energy of detector signals, a number of rates were measured with scalers. A scaler reading is a count of the number of times an event happens in a given time interval. One of the most important of these readings was the ‘good muon event’ or GMU. A GMU was an event that triggered T1 and then had no other T1 event follow within the pileup window. This was counted by finding a coincidence between the end of the pileup gate (EB, caused by \overline{B} turning back on) and the end of the event gate (EEVG). If a second muon *had* triggered T1, the pileup gate would be extended beyond

² \overline{B} was turned off by T1, so there was only a short window, put in by delays and careful timing, when T1 and \overline{B} were in coincidence, see Figure 3.9.

its usual 10 microseconds and would no longer end at the same time as the event gate (see Figure 3.9).

GMU was an important quantity because it monitored the number of *accepted* muons per run and so allowed for comparisons of runs despite fluctuations in beam intensity. Given identical target conditions, electronics and detector positions, the ratio of GMU to any other type of event, be it fusions or muon stops in gold, should remain constant. The extent to which this ratio fluctuates was an indication of how reproducible the targets were, and how truly ‘identical’ were the conditions of similar runs.

3.4 Procedure

The process of making a single target was made as efficient as possible, but it still required a minimum of 4 hours, and could take up to 8 hours, depending on the thickness of the layer and whether the gas required equilibration before being deposited.

3.4.1 the gas-rack: measuring gas for a target

The gas-rack was where targets were measured and mixed; it is the second generation of gas handling systems used by this group, and was first used in 1994. It was designed with the considerations of preparing high-purity, mixed-hydrogen-isotope targets. A commercial unit, the ‘hydrogen generator’ in Figure 3.10, generated protium by electrolysis of deuterium depleted water while the ‘deuterium supply’ was the storage bottle of purified D_2 . The latter was passed through a palladium filter for further purification of the gas before it was measured out into carefully monitored mixing volumes.

The quantity of each type of hydrogen required for a target was calculated in *Tl*. The mixtures were prepared by filling an evacuated mixing-volume of known dimensions with one gas to the desired pressure and sealing it. When only a small amount of the second

gas was required, an adjacent known volume was then filled with this gas to the desired pressure, sealing it also, and finally opening the valves to connect the volumes. If the required amount of the second gas was too large for this method to be safe (i.e. enough to require a pressure greater than atmospheric in the smaller volume), the second gas was carefully bled directly in to the large volume already containing the first gas until the total pressure for the mixture indicated the volume contained 2000Tl of gas.

There were three relevant mixing volumes. Usually the 2000Tl of D₂ and H₂ could be measured out from the 2 litre and the 0.031 litre volumes. When making a target with only 2% deuterium, however, both of the usual volumes were too large, so a third volume of 3.4 ml was used. Composite targets were left at least 2 hours to mix.

The volumes were known to uncertainties of (<1%), except for the smallest volume which was only used to measure the 40Tl of D₂ for the $c_d=.02$ target. This volume had an uncertainty of approximately 2%, as did the pressure gauges. Table 3.1 lists calculated uncertainties of the target concentrations from the runs used in the measurement of the Wolfenstein-Gershtein effect.

C_d (ideal)	C_d (actual, calculated)	error: volumes	error: gauges (max)
0.75	0.7501	0.1%	2%
0.15	0.1501	0.1%	2%
0.02	0.0202	2.7%	2%

Table 3.1: *The calculated target concentrations, including errors.*

All volumes were carefully purged and pumped between uses and, though it is expected that some out-gassing from the walls of the mixing-volume must occur, it did not significantly contributed to contamination.

3.4.2 target depositions

Once the targets reached equilibrium, a deposition line was chosen (either US for the upstream foil or DS for the downstream). The valve VDEP and then the metering valve (VMV) were opened slowly to allow the gas to be gently cryo-pumped through the long line to the inserted diffuser and onto the cold foils in the target vacuum space (see Figure 3.10).

During the depositions it was essential to keep the target cold and the flow moderately slow in order to prevent the solid hydrogen on the target foil from vapourizing. This can happen very quickly, because, if a small amount of frozen hydrogen vaporizes, the pressure will rise suddenly, starting a chain reaction of rising temperature and pressure; in fractions of a second, the entire solid target sublimates. To prevent this, the flow was regulated with a metering valve and the gas was carefully monitored with multiple temperature and pressure gauges to keep the temperature $<4.5\text{K}$ and the pressure below 10^{-6} Torr.

The structure of the solid target is not well understood. It is not known in what exact form the gas condenses into hydrogen-ice, but it is not expected to be significant for the majority of the nuclear and molecular μCF processes. There have been observations of discrepancies between rates measured in solid versus those measured in liquid or gas; some of these are calculated solid state effects, but others are considered to indicate errors in calculating the density of solid hydrogens, rather than a fluctuation in the reduced rates.

observations

Inconsistent behavior was noted during the deposition of the 2% deuterium target. Over the deposition time the ratio of mass 4 to mass 2 isotopes was unstable. Using data from a Residual Gas Analyzer in the vacuum system, the ratio started at 10% and dropped progressively to 0.5%, possibly indicating there was poor mixing of the gases, resulting in an inhomogeneous target. During the other two depositions no such variations were

exhibited, although during the deposition of the 15% target the ratio was 1:10 and for the deposition of the 75% target it was 10:6. Both were lower amounts of deuterium than expected; however the mass spectrometer used tended to be preferential to certain masses and tested an area far enough from the target to make questionable its absolute reliability.

Chapter 4

Presentation and Discussion of Results

The underlying physics involved in the Wolfenstein-Gershtein effect can be quite complicated, but the analysis required to interpret the data was relatively simple. A kinetics code employed all the known rates of reactions in the $pd\mu$ scheme and predicted the relative yields of muons and gammas as fusion products for a given target concentration. The measurement of the final fusion products for three concentrations of the solid, protium-deuterium target was compared to these predictions to test the accuracy of the theory of $pd\mu$ fusion reactions. Finally, the weaknesses in the kinetics code's theory were investigated and the input rates adjusted to obtain a best fit to the data.

Although the ratio of muon yield to gamma yield was deemed the definitive measurement in this experiment because it clearly minimized systematic errors, the individual yields could be fit as well, using an arbitrary normalization to account for detector efficiencies.

The histograms used to calculate these yields were energy histograms which included a delayed electron requirement (see page 35). The fusion gamma data displayed in these his-

tograms were collected from the NaI detector and the fusion muon data from the conversion muon scintillators, while the del-e data were from all three scintillator pairs. Figures 4.1 and 4.2 are examples of these histograms. They display the normalized data from the 75% deuterium target and compare them to the normalized 0% deuterium target (in which no fusions occur).

Each yield was taken to be the sum of the counts within the prescribed energy cut, after background subtraction. The background run was taken with a 2000Tl target of pure protium. All histograms were normalized to ‘GMU’ before subtracting the normalized background, GMU being the number of muons that successfully triggered T1 (see page 39). This normalization allowed for comparisons of runs of different lengths and allowed for fluctuating beam currents. Plotting the ratio of the yields eliminated some of the systematic errors, like inconsistencies in the normalization, and setting the ratio equal to one for the 2% deuterium point canceled unknown efficiencies of the detectors. The latter method was also used to account for the μC scintillator and NaI detector efficiencies when plotting the muon and gamma yields individually.

Figure 4.3 plots the ratio of gammas/muons vs. deuterium concentration while Figures 4.4 and 4.5 show the individual yields plotted against the deuterium concentration.

There are two major differences in how the ratio is fit as compared to fitting the individual yields; one is the effect of a change in normalization (the normalization is relatively insignificant when the ratio is used) and the other is in how each of the reaction rates contributes to the theoretical predictions. By studying Figure 4.6 one can see that the ratio of yields is insensitive to changes in certain rates, like the $p d \mu$ formation rate, the $d d \mu$ formation rates and the rate of muon transfer from p to d nuclei. However, it is affected by the spin-flip rate and the three different fusion rates. The individual yields, on the other hand, are sensitive to absolute changes in fusion yields that depend on the concentration of

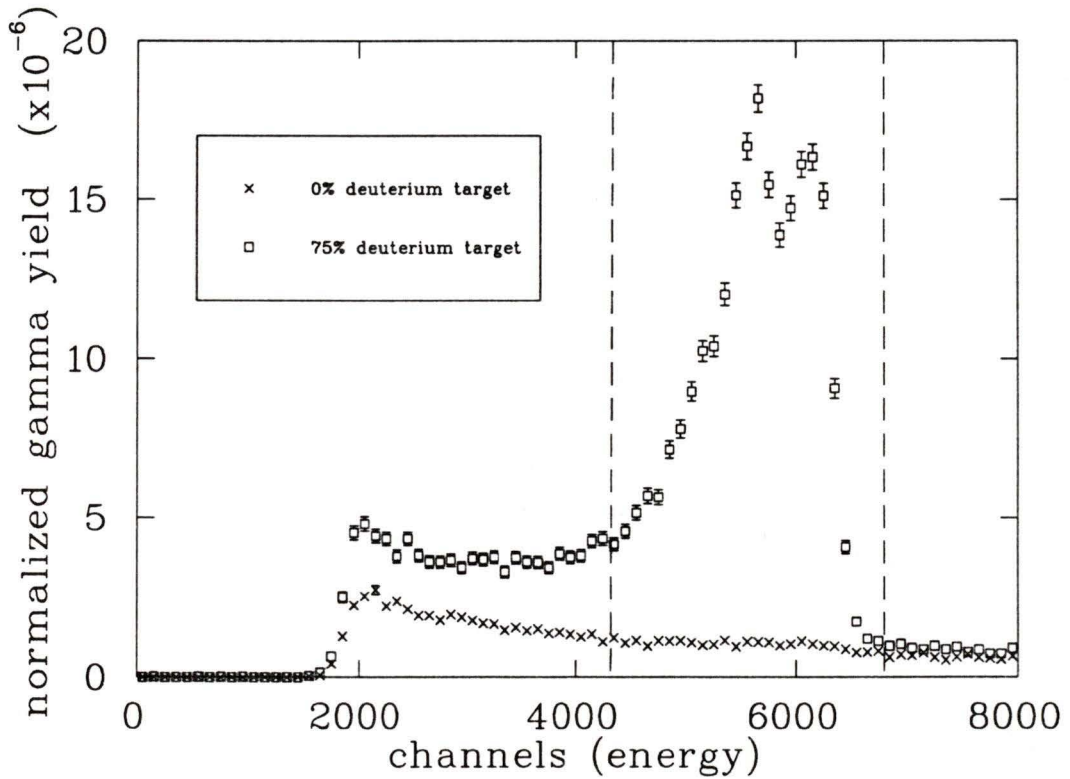


Figure 4.1: The histograms of gamma energies for $c_d=0.75$ and for $c_d=0$ (background), both normalized to GMU. The dashed lines show the energy cut made on the gamma yield sums, from channels 4300-6700 (approximately 3.7 MeV to 6 MeV).

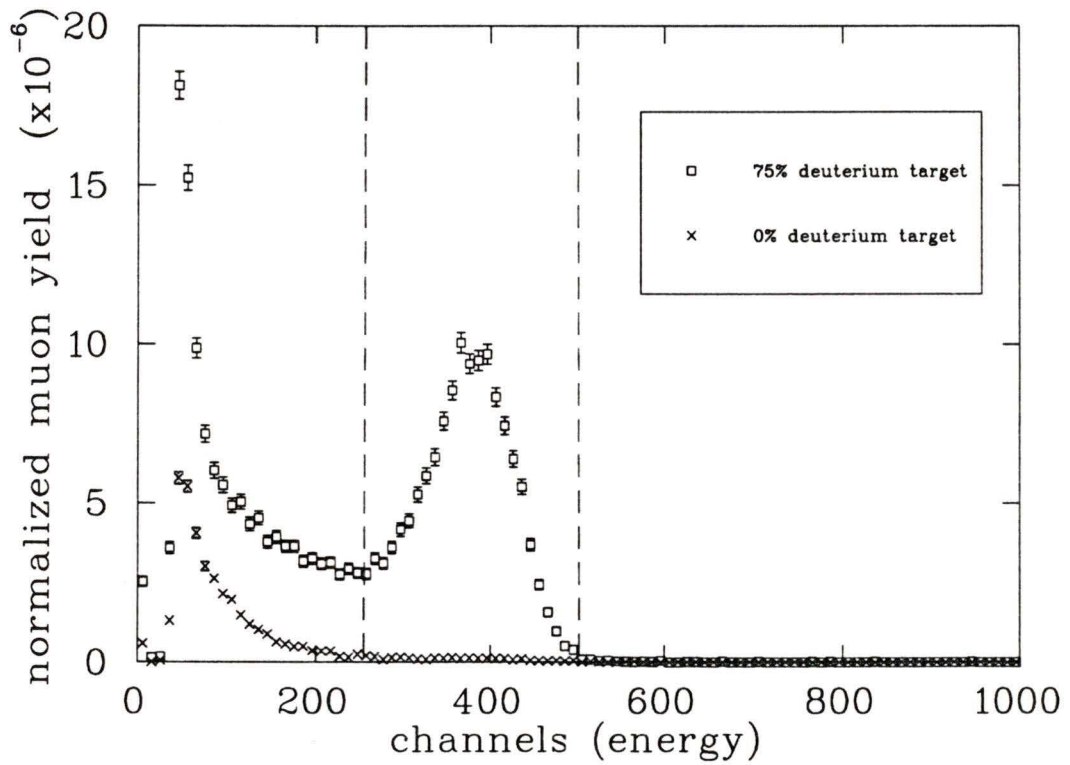


Figure 4.2: The histograms of muon energies for $c_d=0.75$ and $c_d=0$ (background), both normalized to GMU. The dashed lines show the energy cut made on the muon yield sums, from channels 250-500 (approximately 3.2 MeV to 6.5 MeV)

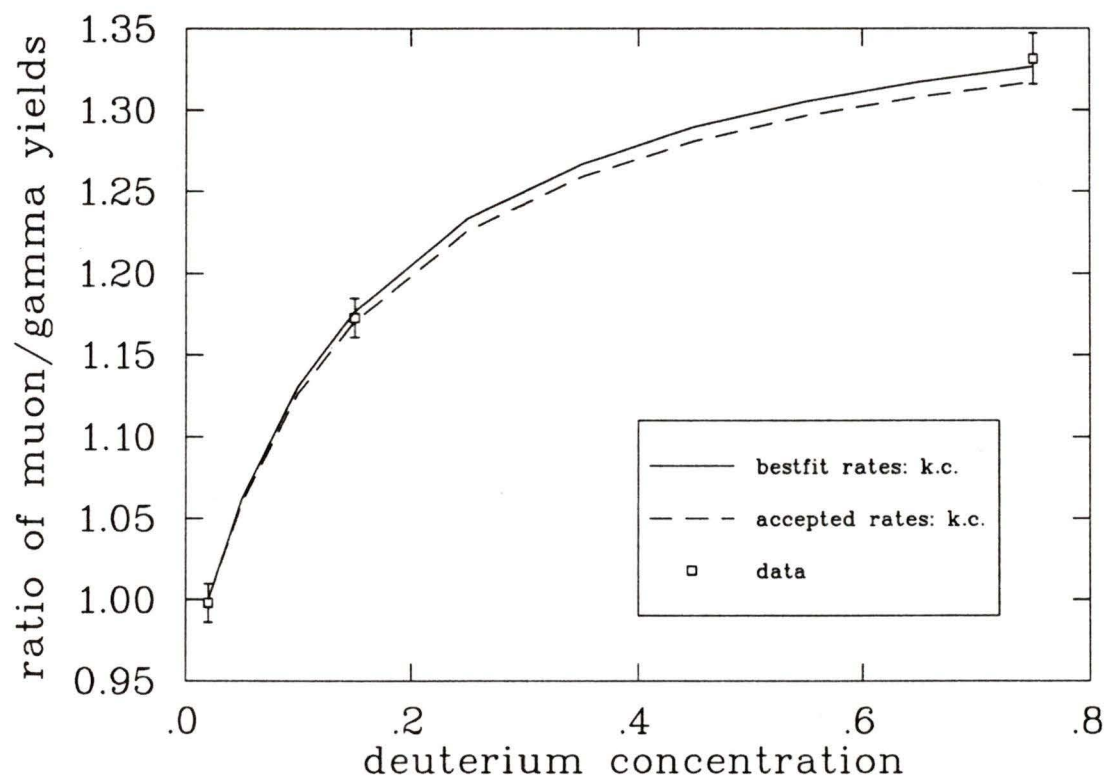


Figure 4.3: *The ratio of muon yield/gamma yields with respect to deuterium concentration, and normalized to GMU. The curves labelled 'k.c.' are theoretical predictions calculated with a kinetics code.*

a target, and to the molecular formation rates.

4.1 Theory: the kinetics code

The kinetics package GENKIN used to obtain the theoretical predictions for comparison with the data was written by Valeri Markushin[38]. This kinetics code is a compilation of ordinary differential equations, each describing one step of the fusion process, which are solved using a Green's function approach. Linked together, these processes can have strong inter-dependencies that make difficult even rough guesses about the possible effects of adjusting any of the rates. The rates initially used in the code are in Table 4.1, while Figure 4.6 shows the fusion schematic that describes how they all fit together.

This code relies on the assumption that the rates are constant in time, which would only be true if the rates had no energy dependence (most of them do not) or the μd atoms were all thermalized (therefore having a simple, thermal energy distribution). Initially the code did not include the possibility of emission of μd atoms from the target (which would require a Monte Carlo simulation, including geometries and stopping distributions, to produce accurate results) because the effect was believed to be insignificant for the deuterium concentrations in question.

Each rate that had a significant effect on the final yield was varied to try to find an optimum set of values. Although the best fit values of the fusion rates can be deduced from fitting the ratio data only, varying some of the other rates that affect the fusion process at an earlier stage was required to correct for discrepancies in the individual yields. See Table 4.1 for the best fit results.

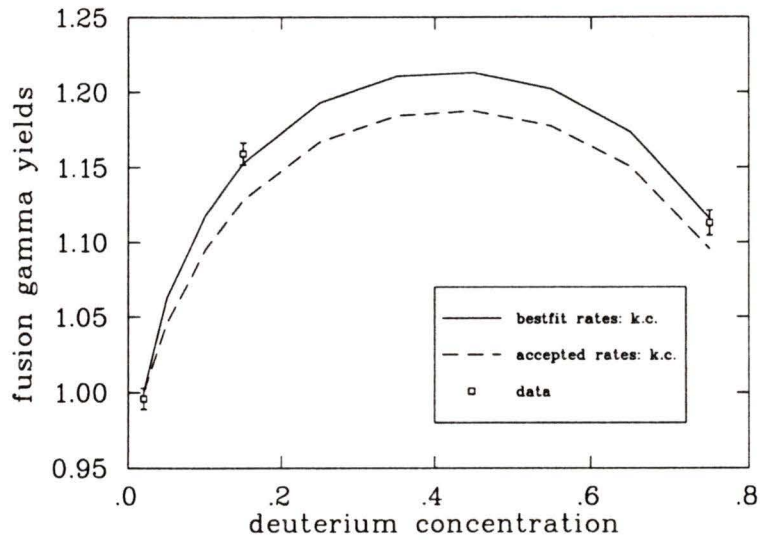


Figure 4.4: The dependence of gamma yield on deuterium concentration, and normalized to GMU. The curves labelled 'k.c.' are theoretical predictions calculated with a kinetics code.

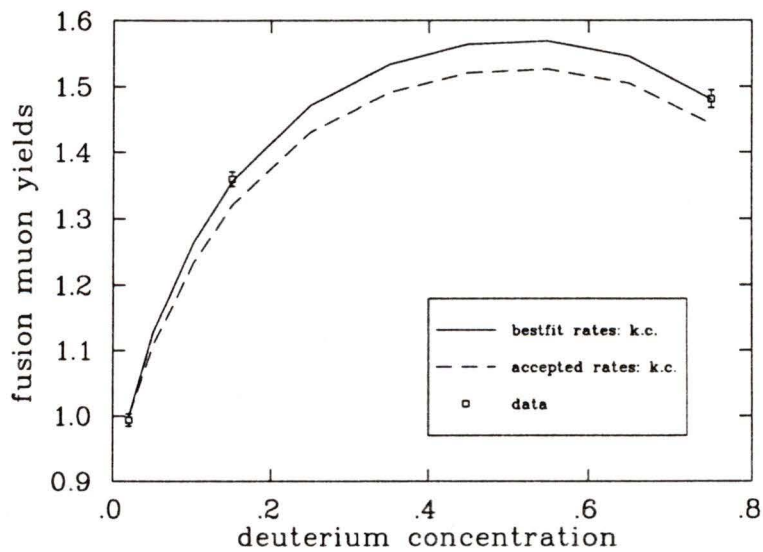


Figure 4.5: The dependence of muon yield on deuterium concentration, and normalized to GMU. The curves labelled 'k.c.' are theoretical predictions calculated with a kinetics code.

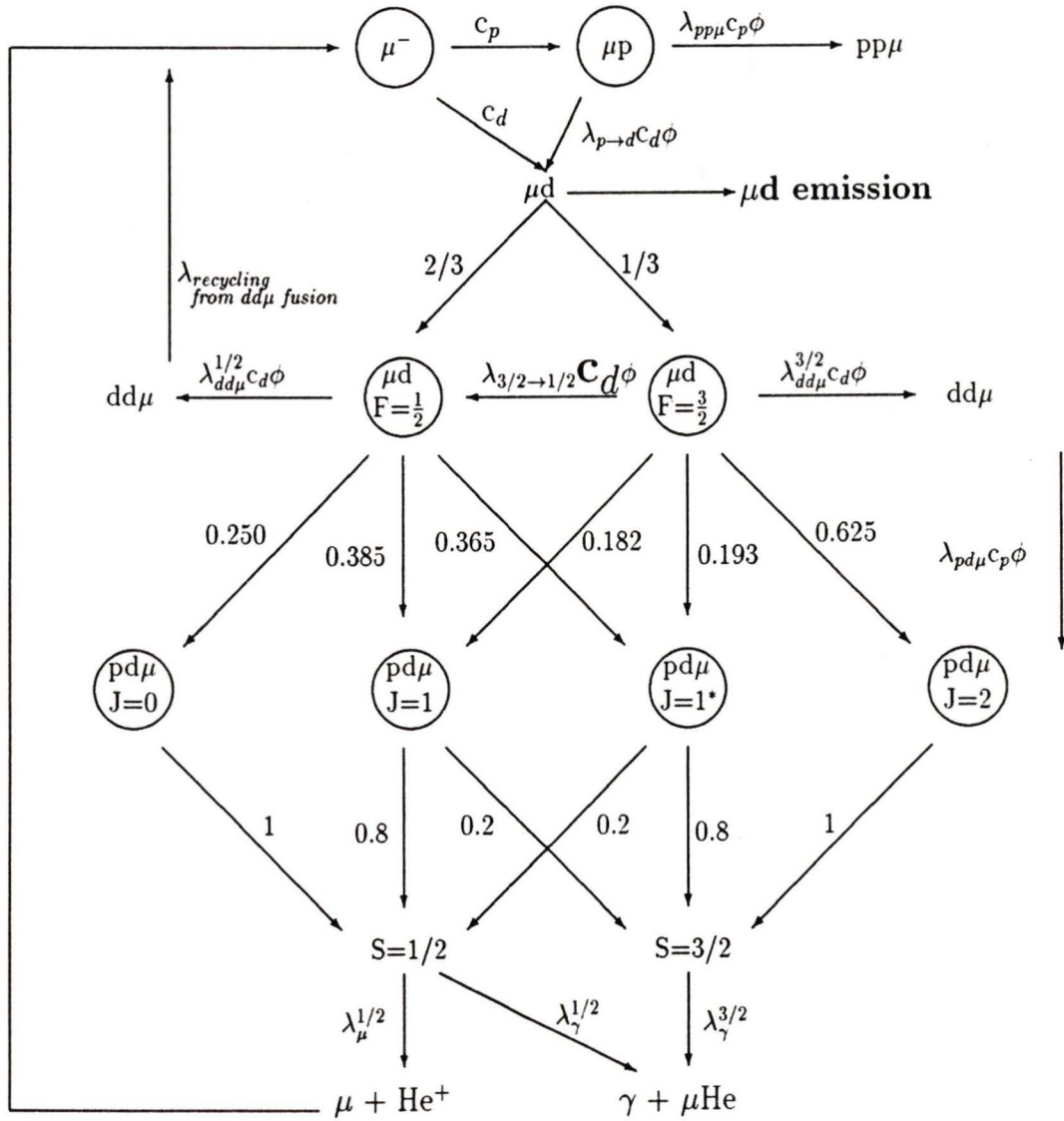


Figure 4.6: The $pd\mu$ fusion schematic: showing the inter-relationship of relevant rates. Note, the emission of μd atoms is NOT included in the kinetics code.

rate	previous measurements ($\times 10^6 \text{s}^{-1}$) [reference]	best fit: ratio ($\times 10^6 \text{s}^{-1}$)	best fit: individual yields ($\times 10^6 \text{s}^{-1}$)
$\lambda_{p \rightarrow d}$	17.5(1.3) $\times 10^3$ [35]	-	5.0(1.0) $\times 10^3$
$\lambda_{3/2 \rightarrow 1/2}$	34.2(8) [34]	33(2)	36(3)
$\lambda_{pp\mu}$	3.56(38) [35]	-	3.5(5)
$\lambda_{pd\mu}$	5.6(2) [30]	-	5.5(3)
$\lambda_{dd\mu}^{1/2}$	3.21(51) [34]	-	-
$\lambda_{dd\mu}^{3/2}$	0.052(8) [34]	-	-
$\lambda_{\mu}^{1/2}$	0.056(6) [31]	-	-
$\lambda_{\gamma}^{1/2}$	0.350(20) [30]	0.400(25)	0.410(30)
$\lambda_{\gamma}^{3/2}$	0.110(10) [30]	0.100(15)	0.100(10)

Table 4.1: *The reaction rates used in theoretical calculations and fits: note those with ‘-’ under the ‘bestfit’ column were not sensitive to the fit. The errors on the ‘bestfit’ values indicate an increase by 1 in the $\chi^2/\text{d.o.f.}$ (degree of freedom) of the fit. The fusion rates in bold were those intended to be fit; they compare favorably with previous measurements.*

4.2 Discussion

The measured ratio of gamma yield to conversion muon yield was well predicted theoretically (see Figure 4.3), however the yields on their own showed a noticeable disagreement with the original predictions. Figures 4.4 and 4.5 show the data compared to two theoretical calculations, one with the rates as measured by previous experiments, the other using adjusted rates, fitted to the data.

Each relevant rate was varied to determine its contribution to improving the theoretical fit. Only one change had a significant effect on *both* yield plots, bringing the theory into agreement with the data without detrimentally affecting the fit to the ratio. When the $p \rightarrow d$ transfer rate of the muon was allowed to vary freely, the best fit results were with a transfer rate of $\approx 1/3$ the measured rate ($5 \times 10^9 \text{ s}^{-1}$ instead of $17.3 \times 10^9 \text{ s}^{-1}$). Since the measured rate has been corroborated in multiple experiments[35, 39, 40], another physical explanation for this discrepancy in the individual yields had to be found. From studying Figure 4.6, it is clear that $\lambda_{p \rightarrow d}$ affects the rate at which μd atoms are produced, particularly at low deuterium concentration; not only does the transfer rate depend on c_d but, at high deuterium concentrations, it is more probable for a μd atom to form directly, rather than through the intermediate step of creating a μp atom. The observable physical outcome would be a reduction in the total number of fusions in targets of low deuterium concentration, as fewer μd atoms result in fewer $pd\mu$ molecules. These observations indicated the importance of a loss mechanism for μd atoms that was not accounted for in the kinetics code; μd emission was recognized as the most likely cause.

Small improvements in the fits were made by increasing the $\lambda_\gamma^{1/2}$ rate to $0.40 \times 10^6 \text{ s}^{-1}$ from $0.35 \times 10^6 \text{ s}^{-1}$, which is in agreement with a preliminary calculation of this rate obtained from fitting the μ and γ time spectra[41]. See Table 4.1 for the comparison of the best fit results of the rates with previous measurements.

4.2.1 μd emission

By using a Monte Carlo simulation it was found that for a 2000 Tl target there is still a significant amount of μd emission from a 2% deuterium target, and a small amount from the other targets. This is because of the Ramsauer-Townsend effect, which results in protium being nearly transparent to μd atoms with energies in the range of our experiment, while deuterium is not. The mean interaction length of a μd atom in pure deuterium is $\approx 0.001\text{mm}$ while at a deuterium concentration of only 2% it becomes 0.05mm, a significant difference when the target is only 0.8mm thick. In a preliminary Monte Carlo calculation, V. Markushin predicted the probabilities shown in Table 4.2 for μd escaping from the various targets used[41].

c_d	probability of μd escaping from a $7\text{mg}/\text{cm}^2$ target
0.02	0.112(3)
0.15	0.033(2)
0.75	0.018(2)

Table 4.2: *The probabilities of μd escaping for a $7\text{mg}/\text{cm}^2$ target of various concentrations; preliminary results using a uniform stopping distribution.*

These results suggest that there would be approximately a 9% difference in the drop in total fusion yield, when comparing losses from the 2% deuterium target to those from the 75% deuterium target. This discrepancy in the data (as compared to the initial theory predictions) is only $\approx 4\%$, however it is difficult to make a direct comparison here for a number of reasons. For a direct comparison the losses from emission would have to be calculated using the time- and energy-dependent rates. Also, the approximation of a uniform stopping distribution results in an over-estimation of escape, particularly for

higher concentrations, because the calculated experimental distribution has more stops in the center region of the target than at the edges, thus increasing the number of μd atoms that have a longer distance to travel before escape[42].

The emission of μd atoms from solid targets of varying concentrations is still being investigated; having a thorough understanding of μd emission is important not only for this measurement, but also for other experiments with similar targets. The calculations presented in Table 4.2 illustrate the trend of the emission losses that was seen in the data, i.e. the significant increase in the loss fraction for the 2% deuterium target.

4.3 Errors

errors in producing the yields and the ratio of yields

Possible sources of systematic error in the analysis were the use of GMU as a normalization, a bias in the energy cuts, and the approximations of the kinetics model used to calculate the theoretical results. The latter is difficult to approximate, but estimates for the errors from analysis techniques have been calculated and included where they were deemed significant. For comparison, statistical errors were less than 1% for the individual yields, and of the order of 1.3% for the muon/gamma ratio, and the background constituted less than 1% of the data.

The assumption used in choosing GMU for a normalization was that, with targets of identical thickness, the same number of fusions was possible, because GMU is proportional to the number of muons that stop in the target and, therefore, to the number of μd atoms formed. With the discovery of the concentration dependent emission of μd atoms from the target, a systematic error in the normalization was predicted; the number of μd atoms available to take part in the fusion cycle would *not* be strictly proportional to GMU times

the concentration dependence of μd formation, but would also be affected by the geometry of the target.

This effect was tested by checking the consistency of the delayed electron spectra with the GMU normalization. Depending on how the μd atom was emitted from the target, the muon's decay electron might have a lower probability of reaching the scintillator pairs. For example: approximately half the μd atoms being lost would have been emitted backwards, in the direction of the gold foil, thus increasing the number of muons capturing onto gold atoms. These losses would reduce the number of observed delayed electrons with respect to GMU. From the comparison of delayed electrons/GMU at $c_d=.02$ to $c_d=.75$ the deviation in GMU as a normalization was calculated to be less than 1.4%. This uncertainty in GMU was included in the analysis. If one assumes that few emitted μd atoms' decay electrons were detected, then the difference in μd emission was equal to the difference in the number of recorded delayed electrons, which was approximately 3.5(5)%.

In investigating the systematic errors of the energy cuts, sums using a variety of energy cuts were made and analyzed for a trend. The deviations were less than the statistical errors of 1%, and thus were considered to be negligible.

errors in producing the fits of the $pd\mu$ fusion rates

The error quoted for each parameter was obtained by observing the change in the $\chi^2/\text{d.o.f.}$ of the fit as that parameter was varied, keeping the others constant. The parameters can be approximated as being decoupled for perturbations of the order of a few percent. Fitting to the individual yields involved serious systematic errors; requiring changes to $\lambda_{p \rightarrow d}$ on the order of 65% was evidence of this. The predictions of the ratio of the fusion yields did not exhibit such large systematic discrepancies with respect to the data.

With the number of parameters involved, certain effects could not be measured ac-

curately; the ratio measurement had almost no sensitivity to some parameters. Most of the rates were held constant once it was determined that the dependence of the measured quantities on these adjustments was insignificant, but, due to the complicated nature of the $pd\mu$ system, it was difficult to be certain which contributions were truly negligible. An example of this was the behavior of the yields with respect to $\lambda_{p \rightarrow d}$; to produce an appreciable improvement in fitting the yields required decreasing the transfer rate by a factor of 2/3. This rate initially appeared to have no significant role in the fit, but changing it was a necessary step towards understanding why fitting the original theoretical prediction to the individual yields failed.

4.4 Conclusions

This investigation of the Wolfenstein-Gershtein effect provided a way of fitting fusion yields, using the $pd\mu$ reaction rates as variable parameters in the fit. The fit of the ratio of fusion yields provided the following values for the reduced fusion rates as measured in a solid target, from both fusion yields: $\lambda_\gamma^{1/2} = 0.400(25) \times 10^6 \text{s}^{-1}$ and $\lambda_\gamma^{3/2} = 0.100(15) \times 10^6 \text{s}^{-1}$. These compare favorably with the previous measurements of $\lambda_\gamma^{1/2} = 0.350(20) \times 10^6 \text{s}^{-1}$ and $\lambda_\gamma^{3/2} = 0.100(10) \times 10^6 \text{s}^{-1}$ which were measured in liquid hydrogen, from the gamma fusion branch only.

The inevitable limitations of the assumptions in the kinetics code make it clear that further analysis of the individual yields would require a Monte Carlo simulation. These data indicate that μd emission is significant, with a difference in μd loss of approximately 4% between the $c_d = .75$ and $c_d = .02$ yields; this is notable for being a larger effect than was previously believed. These results will be useful in testing future models of μd kinetics in solid protium-deuterium targets.

Bibliography

- [1] F.C. Frank, *Nature* 160(1947)525.
- [2] A.D. Sakharov, (*report, Levedev Phys. Inst. Acad. Sci. USSR 1948.*) *Muon Catal. Fusion* 4(1989)235.
- [3] Ya.B. Zeldovich, *Dokl. Akad. Nauk. USSR* 95(1954)493.
- [4] L.W. Alvarez et al., *Phys. Rev. Lett.* 105(1957)1127.
- [5] J.S. Cohen, Review of Fundamental Processes and Applications of Atoms and Ions Ch.2, ed. C.D. Lin, World Scientific, Singapore 1993.
- [6] P. Kammel, Muonic Atoms and Molecules p 111-128, ed. L.A. Schaller and C. Petit-jean, Birkhauser Verlag, Basel 1993.
- [7] T. Kase et al., *Muon Catal. Fusion* 5/6(1990/91)521.
- [8] J.L. Friar, B.F. Gibson and G.L. Payne, *Phys. Rev. Lett.* 66(1991)1827.
- [9] H. Faxen and J. Holtsmark, *Z. Physik* 45(1927)307.
- [10] L.I. Schiff, Quantum Mechanics 2nd ed., McGraw-Hill Book Co. Inc., Toronto, 1955.
- [11] V.V. Kuzminov, Yu.V. Petrov and V.Yu Petrov, *Hyp. Int.* 101/102(1996)197.
- [12] A. Scrinzi et al., *Phys. Rev. A* 47(1993)4691.

- [13] A. Adamczak, *Muon Catal. Fusion* 4(1989)31.
- [14] J. Zmeskal et al., *Phys. Rev. A* 42(1990)1165.
- [15] P. Kammel et al., *Phys. Lett. B* 112(1982)319.
- [16] N. Nagele et al., *Nucl. Phys. A* 493(1989)397.
- [17] C. Petitjean et al., *Hyp. Int.* 101/102(1996)1.
- [18] V.P. Dzhelepov et al., *Sov. Phys. JETP* 74(1992)589-595.
- [19] E.A. Vesman, *JETP Lett.* 5(1967)91.
- [20] M.C. Fujiwara, M.Sc. Thesis, University of British Columbia, 1994.
- [21] S.S. Gershtein, *JETP* 40(1961)698.
- [22] E.J. Bleser et al., *Phys. Rev.* 132(1963)2679.
- [23] S. Bystritski et al., *JETP* 43(1976)606; 44(1976)881.
- [24] W.H. Bertl et al., *Atomkernenergie* 43(1983)184.
- [25] A.V. Matveenکو and L.I. Ponomarev *JETP* 32(1971)871.
- [26] P. Kammel et al., *Phys. Lett. B* 112(1982)319; *Phys. Rev. A* 28(1983)2611.
- [27] J.S. Cohen, D.L. Judd and R.J. Riddell, *Phys. Rev.* 119(1960)397.
- [28] B.P. Carter, *Phys. Rev.* 141(1966)863.
- [29] T.K. Radha and N.T. Meister, *Phys. Rev.* 136(1964)B388.
- [30] C. Petitjean et al., *Muon Catal. Fusion* 5/6(1990/91)199.
- [31] L.N. Bogdanova and V.E. Markushin, *Muon Catal. Fusion* 5/6(1990/91)189.

- [32] J.G. Fetkovitch et al., Phys. Rev. Lett. 4(1960)570.
- [33] M. Schiff, Nuovo Cim. 22(1961)66.
- [34] P.K. Knowles, Ph.D. Thesis, University of Victoria, 1996.
- [35] R. Jacot-Guillarmod et al., Hyp. Int. 101/102(1996)239.
- [36] F. Mulhauser et al., Phys Rev. A 53 5(1996)3069.
- [37] C. Petitjean et al., New results in muon catalyzed pd fusion, paper presented at the μCF -89 Conference, Oxford, report RAL-90-022(1989).
- [38] E.I. Afanasieva, I.V. Balabin and V.E. Markushin, Muon Catal. Fusion 5/6(1990/91)477.
- [39] K. Derrick et al., Phys. Rev. 151(1966)82.
- [40] P. Ackerbauer et al., Hyp. Int. 82(1993)243.
- [41] V. Markushin, private communication.
- [42] J. Wozniak et. al., Hyp. Int. 101/102(1995)573.

Glossary of Terms

ADC	analogue-to-digital converter
AMP	signal amplifier
ATT	signal attenuator
\bar{B}	not-busy signal
B.E.	binding energy
CAMAC	an instrumentation and interface system: Computer Automated Measurement And Control
c_d	deuterium concentration
c_p	protium concentration
CFD	constant fraction discriminator
COIN	multiple signal coincidence module
CPINH	computer inhibit
CS	CAMAC scaler
D(d)	a hydrogen isotope ${}^2_1\text{H}$ atom(nucleus)
del-e	delayed muon decay electron coincidence
DISC	signal discriminator
E1N, E2N	first and second plastic scintillators in front of N (the neutron detector)
EB	end of busy
EEVG	end of event gate
EVGF	event gate
EVTR	general detector event coincidence (from any detector)
EVCL	no event coincidence, event clear

FAN	signal fanout
FIOWA	an analysis program
FWHM	full width at half (peak) maximum
GMU	good muon event (no pile-up during the event)
H(p)	a hydrogen isotope ${}^1_1\text{H}$ atom(nucleus)
hf	hyperfine: relating to the energy difference between spin states
HINH	hardware inhibit
M.C.	Monte Carlo
M.G.	master gate
Molli	a histogramming program
μC	conversion muon
μCF	muon catalyzed fusion
1/N	prescaled trigger
PUG	pile-up gate
ϕ	the density of solid hydrogen
Starburst	the CAMAC-computer interface system
T(t)	a hydrogen isotope ${}^3_1\text{H}$ atom(nucleus)
T1	scintillator in the beam entrance for particle identification
Tl	Torr \times litre
TDC	time-to-digital converter
TOF	time of flight
TRGn	specific detector event trigger (from the n detector, n=Ge, NaI or Neutron)
VDACS	a standard data acquisition program
VS	visual scaler

Vita

Surname: Maier
Given Names: Jennifer Maureen
Place of Birth: Toronto, Ontario, Canada

Educational Institutions Attended:

University of Victoria	1995 to 1997
McGill University	1990 to 1994

Degrees Awarded:

B.Sc. (Honours) McGill University 1994

Honours and Awards:

N.S.E.R.C. Summer Scholarship	1993 & 1994
Canada Scholars Award	1990-92
J.W. McConnell Entrance Scholarship	1990-1992

Publications:

a) publication and refereed conference proceedings:

P.E. Knowles *et al.* **A windowless frozen hydrogen target system**, Nuclear Instruments and Methods (1996) 604-610.

M.C. Fujiwara *et al.* **Characterization of solid hydrogen targets**, Hyperfine Interactions 101/102(1996)641.

G.M. Marshall *et al.* **Time-of-flight measurement of resonant molecular formation in muon-catalyzed dt fusion**, Hyperfine Interactions 101/102(1996)47.

F. Mulhauser *et al.* **Measurement of muon transfer rate λ_{pt} and molecular formation rate $\lambda_{pp\mu}$ in solid hydrogen targets**, Hyperfine Interactions 101/102(1996)229.

b) publications accepted and in-press:

M.C. Fujiwara *et al.* **Characterization of Solid Hydrogen Thin Films via Alpha Particle Energy Loss**, Nuclear Instruments and Methods A.

Partial Copyright License

I hereby grant the right to lend my thesis to users of the University of Victoria Library, and to make single copies only for such users or in response to a request from the Library of any other university, or similar institution, on its behalf or for one of its users. I further agree that permission for extensive copying of this thesis for scholarly purposes may be granted by me or a member of the University designated by me. It is understood that copying or publication of this thesis for financial gain shall not be allowed without my written permission.

Title of Thesis:

The Wolfenstein-Gershtein Effect in Solid Protium-Deuterium Targets

Author:

J. Maureen Maier

May 9th, 1997.